Available online at www.sciencedirect.com

ScienceDirect

Geochimica et Cosmochimica Acta 306 (2021) 98–123

Geochimica et Cosmochimica Acta

www.elsevier.com/locate/gca

The sulfur concentration at anhydrite saturation in silicate melts: Implications for sulfur cycle and oxidation state in subduction zones

Zheng Xu *, Yuan Li

State Key Laboratory of Isotope Geochemistry, Guangzhou Institute of Geochemistry, Chinese Academy of Sciences, Guangzhou 510640, China
CAS Center for Excellence in Deep Earth Science, Guangzhou, 510640, China

Received 28 April 2020; accepted in revised form 13 May 2021; available online 21 May 2021

Abstract

Magmatic sulfur plays an important role in affecting mantle oxidation state, volcanic eruption, formation of ore deposits, and global climate change. To better understand the sulfur cycle in subduction zones and to constrain the sulfur concentration at anhydrite saturation (SCAS) in subducting slab-derived silicate melts, forty-three experiments were conducted at 0.5–5 GPa and 900–1200 °C using a piston cylinder and a multi-anvil apparatus. The experimentally produced silicate melts are rhyodacitic to rhyolitic in composition, and the measured SCAS values range from 170 to 3500 ppm. The SCAS values increase with increasing temperature and the water and CaO content of the silicate melts, but the effect of pressure varying from 0.5 to 5 GPa is negligible. Using our new and all available literature SCAS data ($n = 252$), we tested the accuracy of all previous SCAS models that were calibrated for predicting SCAS in silicate melts at various conditions. We find that the Z–T model (Zajacz and Tsay, 2019) works as the greatest SCAS model in capturing all SCAS data with a mean and median absolute error of 5% and 4%, respectively. The success of the Z–T model in capturing all SCAS data demonstrates its robustness in predicting SCAS in silicate melts relevant for magmatism in subduction zones. Applying the Z–T model to slab melting reveals that slab-derived silicate melts of global subduction zones can dissolve 130–1200 ppm S^{6+}, but they cannot contribute enough sulfur to explain the estimated sulfur abundance (200–500 ppm) in the metasomatized sub-arc mantle, which thus requires the addition of sulfur by slab-derived aqueous fluids. The addition of slab S^{6+} can cause oxidation of the sub-arc mantle in an fO_2 range of FMQ+0.5 to FMQ+2, consistent with the fO_2 values observed for the metasomatized sub-arc mantle peridotites. However, during partial melting of the metasomatized sub-arc mantle, S^{2-} would play as a reducer and the fO_2 of primitive arc basalts cannot be higher than FMQ+0.5 to FMQ+1, which is consistent with the sub-arc mantle fO_2 inferred from the V–Sc, Fe–Zn, V–Ga, and Cu–Re systematics of primitive arc basalts. The fO_2 above FMQ+1 of arc basalts may thus be obtained during magmatic differentiation in the lithosphere. We finally modeled the fate of S^{6+} during the differentiation of parental arc basalts with fO_2 varying from FMQ+0.5 to FMQ+1.5 in a thickened continental arc setting. We find that significant fractions of S^{6+} in the parental arc basalts are converted into S^{2-} and lost in sulfides during arc magmatic differentiation, and the estimated 400 ppm sulfur in Earth's continental crust implies that Earth's continental crust cannot have formed from arc basalts with fO_2 significantly higher than FMQ+0.5 to FMQ+1.

Keywords: Anhydrite; Sulfur cycle; Oxidation state; Arc magmas; Subduction zone

* Corresponding author at: State Key Laboratory of Isotope Geochemistry, Guangzhou Institute of Geochemistry, Chinese Academy of Sciences, Guangzhou 510640, China.
E-mail address: xuzheng@gig.ac.cn (Z. Xu).

https://doi.org/10.1016/j.gca.2021.05.027
0016-7037/

1. INTRODUCTION

As one of the major volatiles in magmas, sulfur (S) plays an important role in magmatic differentiation and degassing, the formation of magmatic-hydrothermal ore deposits, volcanic eruptions, and the short-term global climate change (Botcharnikov et al., 2011; Simon and Ripley, 2011; Oppenheimer et al., 2011; Webster and Botcharnikov, 2011; Audétat and Simon, 2012; Zajacz et al., 2012; Li et al., 2019). In subduction zones, surface S is transported into the mantle through slab subduction (Métrich et al.,1999; de Hoog et al., 2001a), whereas sub-arc mantle S is extracted and released into the atmosphere through mantle melting and magmatic degassing (Wallace, 2005; Webster and Botcharnikov, 2011). The mantle sources of arc magmas are considered to contain 200–500 ppm S (Métrich et al.,1999; de Hoog et al., 2001a), which are higher than the S abundance (~150 ppm) in the depleted mantle (Saal et al., 2002), indicating that the subducting slab must have contributed S to the sub-arc mantle. However, available influx and outflux estimations yielded that more than 80% of the S in the subducting slab may have entered Earth's deep mantle, not sourced by arc volcanos (Hilton et al., 2002; Wallace, 2005; Evans, 2012; Li et al., 2020).

The altered oceanic crust (AOC) and marine sediments contain ~1000–2000 ppm S and are the main S carrier in the subducting slab (Alt and Shanks, 2011; Li and Schoonmaker, 2014). Previous studies investigated the mechanism and efficiency of S transfer from the subducting slab to the sub-arc mantle by focusing on the capacity of slab-derived fluids in dissolving sulfide or sulfate species (Evans, 2012; Jégo and Dasgupta, 2013, 2014; Tomkins and Evans, 2015; Li et al., 2020). However, partial melting of the subducting slab could occur extensively (Defant and Drummond, 1990; Johnson and Plank, 1999; Dasgupta, 2013; Thomson et al., 2016). In hot subduction zones such as Mexico and Peru, the slab surface geothermal crosses the wet solidus of sediment and mid-ocean ridge basalt (MORB) (Fig. 1; Syracuse et al., 2010), which indicates that partial melting could occur for both lithologies during subduction. In subduction zones slab sediments could be detached from the subducting slab forming a buoyant diapir (Behn et al., 2011). Partial melting would occur for this sediment diapir once it enters the hot mantle wedge. Flux of hydrous fluids coming from subjacent lithologies, such as serpentinite, could also trigger partial melting of the sediments and AOC, because the sub-arc slab surface temperatures are above the wet solidus as constrained by the geochemical and geodynamic models (Syracuse et al., 2010; Cooper et al., 2012). In these cases, the capacity of the slab-derived silicate melts in transporting S would dictate the efficiency of S transfer from the slab to the sub-arc mantle and the slab contribution to arc magmatic S outflux. Actually, the estimated S flux (~2.9–12.5 × 10^{12} g/yr) from the subducting slab to the sub-arc mantle using slab-derived fluids is significantly lower than the arc S outflux (~1.4–2.1 × 10^{13} g/yr) (Wallace, 2005; Wallace and Edmonds, 2011; Evans, 2012; Li et al., 2020), which may indicate that slab-derived silicate melts play a globally non-negligible role in transferring slab S to the sub-arc mantle. Furthermore, anhydrite crystals and sulfides were identified in oxidized arc magmatic rocks (Parat et al., 2011; Grondahl and Zajacz, 2017; Chang and Audétat, 2018; Hutchinson and Dilles, 2019; Chen et al., 2020), which indicates that a considerable amount of S^{6+} and S^{2-} is lost in magmatic anhydrite and sulfides and eventually cannot be available for partitioning into fluids or volcanic gasses (Masotta and Keppler, 2015; Zajacz and Tsay, 2019). More importantly, the formation of Earth's continental crust is ultimately related to the magmatism at arcs with thickened crust (Lee et al., 2007; Rudnick and Gao, 2014; Tang et al., 2019; Chen et al., 2020). Therefore, the fate of S during arc magmatic differentiation is closely linked to the S abundance in Earth's continental crust. In this study, in order to understand the efficiency of the S^{6+} transfer from the slab to the sub-arc mantle by slab-derived silicate melts, and the fate of S^{6+} during arc magmatic differentiation, we measure the S concentration at anhydrite saturation (SCAS) in the silicate melts relevant to subduction zones.

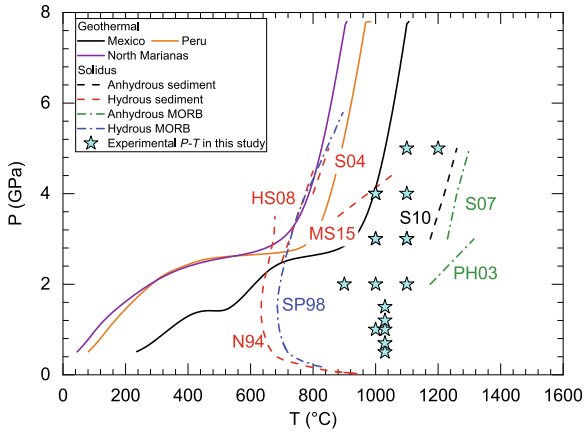

Fig. 1. Comparation of solidus of hydrous/anhydrous MORB and sediments with the geothermal of some typical subduction zones and the present experimental P–T conditions. Slab P–T paths were redrawn from the D80 model in Syracuse et al. (2010). Solidus P–T were taken from Nichols et al. (1994) for N94, Schmidt and Poli (1998) for SP98, Pertermann and Hirschmann (2003) for PH03, Schmidt et al. (2004) for S04, Spandler et al. (2007) for S07, Hermann and Spandler (2008) for HS08, Spandler et al. (2010) for S10, and Mann and Schmidt (2015) for MS15.

The capacity of slab-derived silicate melts in transferring slab S to the sub-arc mantle depends on a number of factors, including temperature, pressure, silicate melt composition, and slab oxygen fugacity (fO_2) (Baker and Moretti, 2011; Jégo and Dasgupta, 2013, 2014). A few studies have focused on determining the S concentration at sulfide saturation (SCSS) in slab-derived silicate melts (Jégo and Dasgupta, 2013, 2014; Prouteau and Scaillet, 2013). The results show that the SCSS in slab-derived silicate melts is rather low (~50–150 ppm) at fO_2 below the FMQ buffer (FMQ = fayalite-magnetite-quartz), indicating a very low capacity of slab-derived silicate melts in transferring slab S to the sub-arc mantle at reduced conditions. In addition to sulfide, anhydrite is another main S-bearing mineral in

the slab (Alt, 1995; Alt et al., 2010; Alt and Shanks, 2011). The flux of slab-derived and S^{6+}-bearing fluids/melts into the sub-arc mantle, as predicted by thermodynamic models, petrographic observations, and isotopic analysis of subduction-related rocks (Mungall, 2002; Debret et al., 2016; 2020; Pons et al., 2016; Bénard et al., 2018; Walters et al., 2020), has been used to explain the high S concentrations and high $\delta^{34}S$ values observed for arc magmas and arc volcanic gasses (Alt et al., 1993; Métrich et al.,1999; de Hoog et al., 2001b; Kagoshima et al., 2015; Pons et al., 2016; Bénard et al., 2018). Several studies have experimentally determined the SCAS in rhyolitic to basaltic melts and calibrated SCAS models to predict SCAS in silicate melts at various conditions (Clemente et al., 2004; Jugo et al., 2005; Li and Ripley, 2009; Baker and Moretti, 2011; Jégo and Dasgupta, 2014; Huang and Keppler, 2015; Masotta and Keppler, 2015; Chowdhury and Dasgupta, 2019; Zajacz and Tsay, 2019). However, most of the previous studies aimed to understand the fate of S^{6+} during magmatic differentiation at shallow crustal conditions. Only Jégo and Dasgupta (2014) measured the SCAS in slab-derived silicate melts by performing four experiments at 2–3 GPa and 950–1050 °C. The results show that the SCAS values are ~700–3000 ppm in rhyodacitic to rhyolitic melts, which are much higher than the SCAS values (~150–1000 ppm) determined for rhyolitic melts at 0.1–0.2 GPa and 900–1000 °C (*e.g.,* Clemente et al., 2004; Masotta and Keppler, 2015; Zajacz and Tsay, 2019). Pressure thus appears to play a positive role in enhancing SCAS, as suggested by the SCAS models of Li and Ripley (2009) and Baker and Moretti (2011). However, the SCAS models of Masotta and Keppler (2015), Chowdhury and Dasgupta (2019), and Zajacz and Tsay (2019) suggest a negligible role of pressure in affecting SCAS. Thus far, the SCAS in slab-derived silicate melts has not been systematically investigated at conditions appropriate for slab melting.

In the past two decades, the S^{6+} cycle in subduction zones has been linked to the oxidation state of the sub-arc mantle and arc magmas (Mungall, 2002; Kelley and Cottrell, 2009; Evans et al., 2012; Bénard et al., 2018). The positive correlation between $Fe^{3+}/\Sigma Fe$ and water content in undegassed, olivine-hosted basaltic melt inclusions was used to argue for a high fO_2 in the metasomatized sub-arc mantle, which was proposed to be caused by fluxing of slab-derived and S^{6+}-bearing fluids/melts (Kelley and Cottrell, 2009, 2012; Evans, 2012; Brounce et al., 2014, 2015). The measured high fO_2 values (FMQ+0.5 to FMQ +1.5) for the metasomatized sub-arc mantle peridotites (Parkinson and Arculus, 1999; Mallmann and O'Neill, 2007; Birner et al., 2017; Bénard et al., 2018) are also ascribed to the addition of slab-derived and S^{6+}-bearing fluids/melts in the sub-arc mantle (McInnes et al., 2001; Bénard et al., 2018). However, the V–Sc, Fe–Zn, V–Ga, and Cu–Re systematics of primitive arc basalts and MORBs imply that the metasomatized sub-arc mantle cannot be 0.5–1 log units more oxidized than the oceanic mantle (Lee et al., 2005, 2010, 2012; Mallmann and O'Neill, 2009; Li, 2018; Feng and Li, 2019). The apparent paradox in the sub-arc mantle fO_2, as constrained using different approaches, remains unresolved.

In this study we perform laboratory experiments at 0.5–5 GPa and 900–1200 °C to determine the SCAS in slab-derived silicate melts. We investigate the effects of temperature, pressure, silicate melt composition, and silicate melt water content on SCAS. The obtained new SCAS data are used to test the accuracy of previous SCAS models. Then the fate of S^{6+} during slab melting and arc magmatic differentiation, and the role played by slab S^{6+} in affecting the oxidation state in subduction zones are discussed.

2. METHODS

2.1. Starting materials

Three different silicates were used in this study; the first one is a natural rhyolite, the second one is a synthetic hydrous rhyolite with ~5 wt.% water, and the third one is a synthetic andesite. Both the natural rhyolite and synthetic andesite are nominally water-free, and the major element compositions of all three silicates are listed in Table 1. The rhyolite was chosen to be representative of silicate melts produced by partial melting of the subducting slab sediments and/or AOC (Schmidt et al., 2004; Hermann and Spandler, 2008; Skora and Blundy, 2010; Tsuno and Dasgupta, 2012; Mann and Schmidt, 2015; Jégo and Dasgupta, 2013; 2014). The andesite was similar in composition to the silicate melt produced by partial melting of AOC at 1350 °C and 5 GPa (Spandler et al., 2008). Under the present experimental *P-T* conditions (Fig. 1), partial melting of the andesite would produce rhyodacitic melts as produced in previous experiments simulating partial melting of the subducting AOC (Jégo and Dasgupta, 2013, 2014). The synthetic hydrous rhyolite and andesite were prepared from high-purity oxides, carbonates, and aluminum hydroxide. SiO_2, TiO_2, Al_2O_3, and MgO powder were each heated over night at 1000 °C, $CaCO_3$ at 200 °C, and Na_2CO_3 and K_2CO_3 at 110 °C to minimize adsorbed water contents. The chemical powder of SiO_2, TiO_2, Al_2O_3, MgO, Na_2CO_3 and K_2CO_3 were mixed and grinded in acetone in a mortar for about one hour, and then dried at room temperature. Then the dried mixture was heated in a muffle at 1000 °C overnight for decarbonation. The mixture was subsequently mixed with FeO, MnO, and P_2O_5 for the

Table 1
Major element compositions of the starting silicates (in wt.%).

	Andesite	Rhyolite	Hydrous rhyolite
SiO_2	61.6	76.5	71.6
TiO_2	6.0	0.1	0.1
Al_2O_3	12.8	13.3	12.6
FeO_t	4.9	0.6	0.7
MnO	0.0	0.1	0.1
MgO	1.1	0.1	0.1
CaO	4.2	0.5	0.4
Na_2O	2.2	4.3	4.2
K_2O	5.8	4.7	5.0
P_2O_5	0.9	0.0	0.0
H_2O	0.0	0.0	5.2
Total	99.5	100.2	100.0

preparation of andesite, or with FeO, MnO, and $Al(OH)_3$ for the preparation of hydrous rhyolite. The final mixture was then grinded in acetone in a mortar for another one hour and dried at room temperature. All starting silicate powder was stored in a vacuumed oven at 100 °C.

The starting silicate and high-purity anhydrite ($CaSO_4$) were mixed in a proportion of ~1.5:1, which were then loaded into Au capsules. The high proportion of anhydrite ensured the saturation of anhydrite in the experiments but would not affect the measured SCAS. To investigate the effect of water on SCAS, ~3–10 wt.% H_2O were added into the Au capsules using a micro-syringe for the Set-1 and Set-2 experiments (Table 2), in which the nominally dry rhyolite and andesite were used as the starting silicate, respectively. In the Set-3 experiments where the hydrous rhyolite was used (Table 2), no additional water was added to try to obtain a constant water content in the silicate melt. In the Set-4 experiments (Table 2), the dry rhyolite was used as the starting silicate, without adding water in the Au capsules.

2.2. High-pressure experiments

The experiments at 0.5–4 GPa were performed in an end-loaded solid media piston cylinder apparatus (Max Voggenreiter LPC250), using 1/2-inch Talc–Pyrex assemblies and graphite heaters. Pressure of the experiments was estimated from the hydraulic pressure that was calibrated against the quartz–coesite and kyanite–sillimanite transitions with a 20% friction correction applied. The pressure uncertainty was estimated to be better than 0.1 GPa. Temperature of the experiments was monitored by S-type ($Pt–Pt_{90}Rh_{10}$) thermocouples with an estimated temperature uncertainty of ±10 °C.

The experiments at 5 GPa were carried in an SP-1000 Kawaii-type multi-anvil apparatus. Tungsten carbide (WC) anvils with 11-mm truncated edge lengths, together with a Cr_2O_3-doped MgO octahedron (18 mm edge length) as the pressure medium, were used to generate high pressures. $LaCrO_3$ tubes with outer and inner diameters of 6 and 3 mm were used as heaters. The sample Au capsule was located into a MgO tube with outer and inner diameters of 3 and 2 mm and covered with a 0.05 mm thick tungsten slice to prevent the destruction of capsule by the thermocouple. Experimental pressure was estimated from the hydraulic pressure using calibrations based on the phase transitions of Bi, ZnS, and Mg_2SiO_4 polymorphs. Temperature of the experiments was monitored by C-type ($W_{95}Re_{05}–W_{74}Re_{26}$) thermocouples with an estimated temperature uncertainty of ±10 °C.

Durations of the experiments ranged from 38 to 48 hours, which we found are sufficient for attaining equilibrium as evidenced by the homogeneous distribution of major elements and S in the silicate melts (see below) and as evidenced by previous experiments at similar temperatures (Zajacz and Tsay, 2019). The experiments were quenched by turning off electrical power to the heaters. The recovered samples capsules were cut into two halves using a diamond wire saw; one half polished for optical observations, electron microprobe analyses, and Raman measurements, and the other half of some samples double-sides polished for FTIR measurements.

2.3. Analysis

2.3.1. Electron microprobe

Major element compositions and the sulfur concentrations of the quenched silicate melts were analyzed using a JEOL JXA-8230 electron microprobe. Accelerating voltage of 15 kV, beam current of 10 nA and beam size of 10 μm were used as the analytical conditions for major elements. The peak counting time was 10 s for Na and K, 20 s for Si, Fe, Ca and Al, 40 s for Mg and Ti, and 60 s for Mn. These analytical conditions are similar to those used in previous studies for measuring SCAS in hydrous rhyolitic melts (Jégo and Dasgupta, 2013, 2014; Masotta and Keppler, 2015; Zajacz and Tsay, 2019). Test on a few samples from the Set-3 experiments (Table 2) using a beam current of 5 nA yielded consistent Na_2O and K_2O contents within analytical uncertainties. Diopside was used as standard for Si and Ca, whereas rutile, obsidian glass, magnetite, rhodonite, olivine, albite and orthoclase were used as standards for Ti, Al, Fe, Mn, Mg, Na, and K, respectively. For measuring sulfur, accelerating voltage of 15 kV, beam current of 70 nA, and beam size of 10 μm were used, and the peak counting time was 60 s. Both pyrite and barite standards were used to calibrate the instruments. A synthetic basaltic glass K71 and an obsidian glass were repeatedly measured as external standards to check the accuracy of the analysis, although both glasses are nominally anhydrous.

Major element composition of clinopyroxene, omphacite, coesite, and anhydrite was analyzed using a JEOL JXA-8230 electron microprobe. Accelerating voltage of 15 kV, beam current of 20 nA, and beam size of 1 μm were used as the analytical conditions for major elements. The peak counting time was 10 s for Na and K, 20 s for Si, Mg, Fe, Ca and Al, and 40 s for Mn and Ti. Diopside was used as standard for Si, Mg, and Ca, whereas rutile, almandine garnet, magnetite, rhodonite, albite, orthoclase, and barite were used as standards for Ti, Al, Fe, Mn, Na, K, and S, respectively.

2.3.2. FTIR and Raman spectroscopy

Some of the quenched silicate melts were chosen for water concentration analysis using a JASCO FT/IR-6100 FTIR. The quenched silicate melts (glasses) show typical absorption peaks of 5230 cm^{-1}, 4520 cm^{-1} and 3600 cm^{-1}. The former two bands were used to calculate the total water contents following the Lambert–Beer law:

$$C_{H_2O_t} = 18.015 \times A_{5230}/(\rho \times d \times \varepsilon_{5230}) + 18.015 \times A_{4520}/(\rho \times d \times \varepsilon_{4520}) \quad (1)$$

where $C_{H_2O_t}$, A, ρ, d and ε refer to the water concentration in wt.%, height of the peak in cm^{-1}, density of the melt in g L^{-1}, thickness of the sample in mm, and absorption coefficient in mol^{-1} cm^{-1}, respectively. The ε values corresponding to the water 5230 and 4520 cm^{-1} peaks were taken from Ohlhorst et al. (2001). Density of the melt was calculated using the following linear equation:

$$\rho = -12.88C_{H_2O_t} + 2521.6 \quad (2)$$

Table 2
Summary of the experimental conditions and products.

Run No.	Pressure (GPa)	Temperature (° C)	Run duration hours	Starting materials	Run products	Silicate melt SCAS (ppm)	[a]H_2O in silicate melt (wt.%)	[b]H_2O in silicate melt (wt.%)
Set-1 Experiments on rhyolite and water								
RSCAS-1	1	1000	40	Rhyolite + anhydrite + H_2O	Gl + Anhy	192 ± 66	6.03 ± 0.43	
RSCAS-2	1	1000	40	Rhyolite + anhydrite + H_2O	Gl + Anhy	521 ± 59	9.85 ± 0.59	
RSCAS-3	1	1000	40	Rhyolite + anhydrite + H_2O	Gl + Anhy	248 ± 45	3.63 ± 0.56	
RSCAS-4	1	1000	40	Rhyolite + anhydrite + H_2O	Gl + Qtz + Anhy	885 ± 24	7.78 ± 0.40	
RSCAS-6	2	1000	40	Rhyolite + anhydrite + H_2O	Gl + Qtz + Cpx + Anhy	1749 ± 80	8.67 ± 0.98	
RSCAS-7	2	1000	40	Rhyolite + anhydrite + H_2O	Gl + Anhy	1835 ± 170	10.94 ± 1.09	
RSCAS-8	2	1000	40	Rhyolite + anhydrite + H_2O	Gl + Anhy	3478 ± 302	11.61 ± 0.50	
RSCAS-9	3	1000	39	Rhyolite + anhydrite + H_2O	Gl + Anhy	2749 ± 321	11.28 ± 1.17	
RSCAS-10	3	1000	39	Rhyolite + anhydrite + H_2O	Gl + Qtz + Cpx + Anhy	3012 ± 350	12.61 ± 0.89	
RSCAS-13	4	1000	48	Rhyolite + anhydrite + H_2O	Gl + Coe + Cpx + Po + Anhy	2744 ± 171	11.84 ± 0.59	11.34 ± 0.75
RSCAS-14	4	1000	48	Rhyolite + anhydrite + H_2O	Gl + Coe + Cpx + Po + Anhy	3247 ± 238	10.04 ± 0.50	10.87 ± 0.54
RSCAS-15	2	900	41	Rhyolite + anhydrite + H_2O	Gl + Qtz + Cpx + Anhy	336 ± 37	7.98 ± 0.46	
RSCAS-16	2	900	41	Rhyolite + anhydrite + H_2O	Gl + Qtz + Cpx + Anhy	322 ± 34	7.84 ± 0.56	
RSCAS-17	2	900	40	Rhyolite + anhydrite + H_2O	Gl + Qtz + Cpx + Anhy	325 ± 14	7.10 ± 0.40	6.56 ± 0.93
RSCAS-18	2	900	40	Rhyolite + anhydrite + H_2O	Gl + Qtz + Cpx + Anhy	341 ± 23	7.05 ± 0.40	7.05 ± 0.22
RSCAS-19	2	1100	40	Rhyolite + anhydrite + H_2O	Gl + Qtz + Cpx + Anhy	374 ± 48	4.24 ± 0.00	4.19 ± 0.12
RSCAS-20	2	1100	40	Rhyolite + anhydrite + H_2O	Gl + Qtz + Cpx + Anhy	472 ± 34	4.19 ± 0.23	
RSCAS-21	2	1100	40	Rhyolite + anhydrite + H_2O	Gl + Qtz + Cpx + Anhy	3291 ± 663	10.61 ± 0.71	
RSCAS-22	2	1100	40	Rhyolite + anhydrite + H_2O	Gl + Anhy	3337 ± 488	10.02 ± 0.52	10.33 ± 0.18
RSCAS-23	3	1100	40	Rhyolite + anhydrite + H_2O	Gl + Qtz + Cpx + Anhy	922 ± 28	4.63 ± 0.15	
RSCAS-24	3	1100	40	Rhyolite + anhydrite + H_2O	Gl + Qtz + Cpx + Anhy	1007 ± 36	7.01 ± 0.29	
RSCAS-25	3	1100	40	Rhyolite + anhydrite + H_2O	Gl + Anhy	1406 ± 76	9.38 ± 0.42	
RSCAS-26	3	1100	40	Rhyolite + anhydrite + H_2O	Gl + Anhy	2956 ± 157	8.70 ± 0.42	
Set-2 Experiments on andesite and water								
ASCAS-1	3	1000	40	Andesite + anhydrite + H_2O	Gl + Cpx + Rt + Anhy	750 ± 41	11.04 ± 0.57	
ASCAS-2	3	1000	40	Andesite + anhydrite + H_2O	Gl + Cpx + Rt + Anhy	614 ± 50	10.11 ± 0.42	
ASCAS-3	3	1100	40	Andesite + anhydrite + H_2O	Gl + Cpx + Rt + Anhy	924 ± 17	12.03 ± 0.42	
ASCAS-4	3	1100	40	Andesite + anhydrite + H_2O	Gl + Cpx + Rt + Anhy	528 ± 67	9.68 ± 0.70	
ASCAS-5	4	1000	40	Andesite + anhydrite + H_2O	Gl + Cpx + Rt + Anhy	1065 ± 67	9.67 ± 1.87	
ASCAS-6	4	1000	40	Andesite + anhydrite + H_2O	Gl + Cpx + Rt + Anhy	954 ± 170	11.70 ± 3.08	
ASCAS-7	4	1100	40	Andesite + anhydrite + H_2O	Gl + Cpx + Rt + Anhy	1448 ± 269	3.86 ± 0.50	
ASCAS-8	4	1100	40	Andesite + anhydrite + H_2O	Gl + Cpx + Rt + Anhy	1335 ± 168	4.17 ± 0.12	
ASCAS-9	5	1100	40	Andesite + anhydrite + H_2O	Gl + Coe + Cpx + Rt + Anhy	2265 ± 280	7.40 ± 1.05	
ASCAS-10	5	1200	38	Andesite + anhydrite + H_2O	Gl + Coe + Cpx + Rt + Anhy	2512 ± 192	7.56 ± 0.49	
Set-3 Experiments on hydrous rhyolite at 1030 °C								
RSCAS-32	0.5	1030	40	Hydrous rhyolite + anhydrite	Gl + Anhy	260 ± 35	3.30 ± 0.18	
RSCAS-28	0.7	1030	40	Hydrous rhyolite + anhydrite	Gl + Anhy	193 ± 14	5.18 ± 0.33	
RSCAS-30	1	1030	40	Hydrous rhyolite + anhydrite	Gl + Anhy	241 ± 8	5.81 ± 0.38	
RSCAS-36	1.2	1030	40	Hydrous rhyolite + anhydrite	Gl + Anhy	470 ± 47	5.22 ± 0.25	

RSCAS-34	1.5	1030	40	Hydrous rhyolite + anhydrite	Gl + Anhy	289 ± 23	5.83 ± 0.45	
Set-4 Experiments on dry rhyolite at 1030 °C								
RSCAS-31	0.5	1030	40	Dry rhyolite + anhydrite	Gl + Anhy	614 ± 48		
RSCAS-27	0.7	1030	40	Dry rhyolite + anhydrite	Gl + Anhy	210 ± 25		
RSCAS-29	1	1030	40	Dry rhyolite + anhydrite	Gl + Qtz + Anhy	544 ± 23		
RSCAS-35	1.2	1030	40	Dry rhyolite + anhydrite	Gl + Qtz + Anhy	330 ± 46		
RSCAS-33	1.5	1030	40	Dry rhyolite + anhydrite	Gl + Qtz + Anhy	171 ± 2		

Gl: glass; Cpx: clinopyroxene; Qtz: quartz; Coe: coesite; Rt: rutile; Anhy: anhydrite; Po: pyrrhotite.
[a] H_2O calculated by difference from EPMA total to 100 wt.%.
[b] H_2O measured by FTIR.

which was constructed by fitting the dacitic melt data from Ohlhorst et al. (2001). The H_2O concentration in the silicate melt was calculated using Eqs. (1) and (2) and an iterative approach.

Laser Raman spectra were collected using the Horiba Xplora laser Raman microscope to identify mineral phases. An Ar^+ ion laser with an excitation wavelength of 532 nm was operated at 44 mW. The scanning range of the spectra was set to be 100–4000 cm^{-1} and the accumulation time for each scan was 10 s. A spectral resolution of 0.65 cm^{-1} and beam diameter of 1 μm were used. The Raman peak at 520.7 cm^{-1} of a monocrystalline silicon sample was used to calibrate the instrument.

3. RESULTS

3.1. Sample petrography

Four sets of experiments, including totally forty-three experiments, were done at 0.5–5 GPa and 900–1200 °C. The experimental conditions and run products are summarized in Table 2. Some representative textures are shown in Fig. 2. Anhydrite crystals and silicate melt were present in all experiments. For the Set-1 experiments starting with rhyolite and water (Set-1 experiments on hydrous rhyolite in Table 2), quartz crystals (<~4% in volume) formed in some experiments at 2–3 GPa, while coesite crystals formed in the experiments at 4 GPa. Jadeite crystals formed in some experiments at 2–4 GPa. In addition, a few small pyrrhotite crystals (<15 μm) were found in runs RSCAS-13 and RSCAS-14 at 4 GPa, but they were not found in the other experiments. For the Set-2 experiments starting with andesite and water (Set-2 experiments on hydrous andesite in Table 2), crystals of clinopyroxene and rutile were observed in the experiments at 3–4 GPa, and crystals of clinopyroxene, rutile, and coesite were observed in the experiments at 5 GPa. For the Set-3 experiments starting with hydrous rhyolite (Set-3 experiments on hydrous rhyolite at 1030 °C in Table 2), no silicate crystals were found. For the Set-4 experiments starting with dry rhyolite at 1030 °C (Set-4 experiments on dry rhyolite at 1030 °C in Table 2), quartz crystals were observed in three experiments at 1–1.5 GPa. Note that the Set-3 and Set-4 experiments were performed at a fixed temperature of 1030 °C. We below focus on the major element compositions and S concentrations of the silicate melts.

3.2. Major element composition of the silicate melts

Major element compositions of the silicate melts are given in Table 3, and major element compositions of the clinopyroxene, coesite, and anhydrite crystals measured for some experiments are given in Table S1. In the Set-1 experiments starting with rhyolite and water at 1–4 GPa (Table 2), the silicate melts on the dry basis had major element compositions similar to those of the starting rhyolite. Fig. 3 shows the variation of SiO_2, Al_2O_3, CaO, Na_2O, and K_2O as a function of pressure at various temperatures. In general, the SiO_2 and Na_2O contents (73–78 wt.% and 1.8–4.2 wt.%, respectively) decrease with increasing pres-

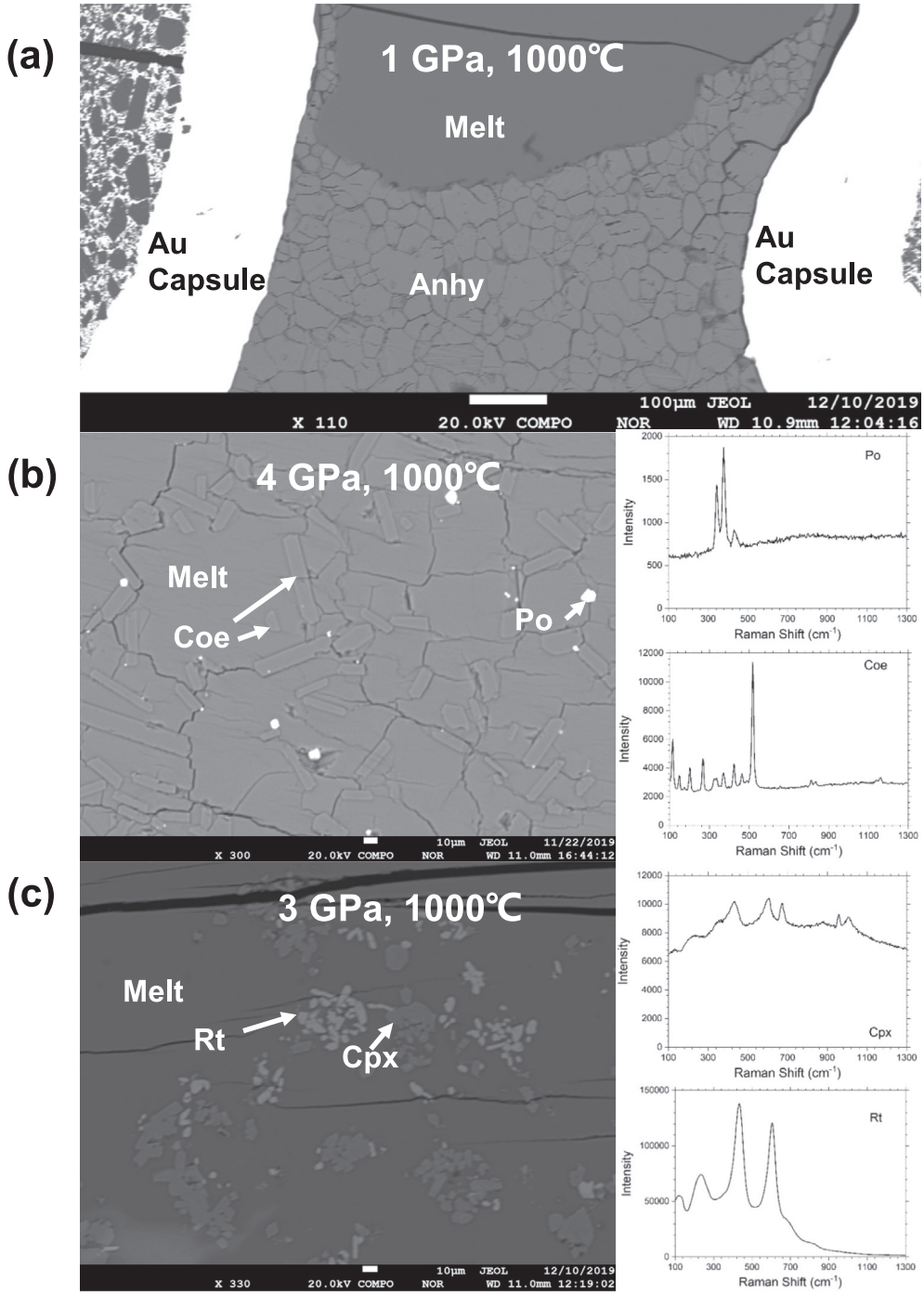

Fig. 2. BSE-microphotographs of typical run products. (a) RSCAS-2 (1 GPa, 1000 °C) showing coexisting anhydrite crystals and silicate melt. (b) RSCAS-14 (4 GPa, 1000 °C) showing coexisting coesite and pyrrhotite crystals embedded in the silicate melt. (c) ASCAS-1 (3 GPa, 1000 °C) showing coexisting clinopyroxene and rutile crystals embedded in the silicate melt. Phase abbreviations: Cpx = clinopyroxene; Coe = coesite; Rt = rutile; Anhy = anhydrite; Po = pyrrhotite. Raman spectral for some of the produced crystals were attached.

sure because of the crystallization of quartz + jadeite or coesite + jadeite at pressures higher than 2 GPa (Fig. 3a and d). The CaO content (0.5–2.1 wt.%) generally increases with increasing pressure (Fig. 3c). The K_2O content (4.2–6.0 wt.%) in the silicate melt only slightly increases with increasing pressure (Fig. 3e). At a given pressure, the variation of the major element composition can be ascribed to the degree of crystallization controlled by the experimental temperature and sample water content.

In the Set-2 experiments starting with andesite and water at 3–5 GPa (Table 2), the produced silicate melts were rhyodacitic. Compared to the starting andesite, the silicate melts had higher contents of SiO_2 (67–75 wt.%) and K_2O (7.5–11.8 wt.%) but lower contents of CaO (0.9–2.1 wt.

Table 3
Compositions of the quenched silicate melts (in wt.%).

Run No.	SiO_2	TiO_2	Al_2O_3	FeO_t	MnO	MgO	CaO	Na_2O	K_2O	SO_3	H_2O
Set-1 Experiments on rhyolite and water											
RSCAS-1	77.94	0.07	11.99	0.65	0.08	0.07	0.45	3.92	4.83	0.05	6.03
1σ	0.42	0.03	0.13	0.08	0.02	0.03	0.06	0.15	0.08	0.02	0.43
RSCAS-2	78.78	0.08	11.80	0.60	0.04	0.07	0.47	3.43	4.72	0.13	9.85
1σ	0.55	0.03	0.13	0.05	0.02	0.01	0.08	0.14	0.05	0.01	0.59
RSCAS-3	77.65	0.09	11.80	0.51	0.06	0.12	0.65	3.85	5.26	0.06	3.63
1σ	0.50	0.01	0.34	0.07	0.06	0.03	0.16	0.06	0.08	0.01	0.56
RSCAS-4	76.46	0.08	12.11	0.23	0.04	0.59	1.29	4.15	5.06	0.22	7.78
1σ	0.38	0.02	0.24	0.02	0.03	0.05	0.09	0.18	0.07	0.01	0.40
RSCAS-6	75.30	0.08	12.95	0.04	0.05	0.04	2.07	4.22	5.24	0.44	8.67
1σ	1.63	0.03	0.68	0.03	0.03	0.02	0.26	0.24	0.23	0.02	0.98
RSCAS-7	78.01	0.08	11.95	0.52	0.08	0.05	1.06	3.43	4.83	0.46	10.94
1σ	0.81	0.02	0.25	0.06	0.03	0.01	0.07	0.25	0.11	0.04	1.09
RSCAS-8	77.60	0.05	12.03	0.57	0.06	0.05	1.36	3.40	4.87	0.87	11.61
1σ	0.55	0.02	0.38	0.10	0.03	0.01	0.15	0.21	0.11	0.08	0.50
RSCAS-9	77.79	0.06	12.04	0.57	0.06	0.06	1.22	3.41	4.79	0.69	11.28
1σ	1.01	0.03	0.25	0.05	0.02	0.01	0.09	0.16	0.15	0.08	1.17
RSCAS-10	74.38	0.07	15.87	0.40	0.05	0.06	1.43	3.08	4.65	0.75	12.61
1σ	1.41	0.03	1.58	0.08	0.04	0.01	0.11	0.10	0.09	0.09	0.89
RSCAS-13	76.55	0.09	13.98	0.07	0.06	0.07	1.55	2.58	5.04	0.69	11.34
1σ	0.56	0.01	0.18	0.03	0.01	0.01	0.06	0.13	0.08	0.04	0.75
RSCAS-14	75.19	0.10	14.21	0.03	0.04	0.07	1.72	2.63	5.99	0.81	10.04
1σ	0.46	0.01	0.17	0.02	0.01	0.01	0.10	0.13	0.12	0.06	0.50
RSCAS-15	75.01	0.10	15.15	0.61	0.08	0.10	0.53	2.98	5.44	0.08	7.98
1σ	0.50	0.01	0.13	0.10	0.01	0.01	0.02	0.11	0.14	0.01	0.46
RSCAS-16	74.92	0.10	15.16	0.55	0.07	0.08	0.58	3.07	5.46	0.08	7.84
1σ	0.60	0.01	0.20	0.04	0.01	0.01	0.04	0.04	0.12	0.01	0.56
RSCAS-17	75.27	0.10	14.77	0.44	0.07	0.08	0.61	3.10	5.54	0.08	7.10
1σ	0.44	0.01	0.06	0.02	0.01	0.02	0.04	0.10	0.08	0.00	0.40
RSCAS-18	75.25	0.10	14.90	0.49	0.06	0.08	0.55	3.08	5.48	0.09	7.05
1σ	0.41	0.01	0.15	0.02	0.01	0.01	0.02	0.08	0.06	0.01	0.40
RSCAS-19	75.84	0.09	14.04	0.63	0.05	0.07	0.73	3.45	5.10	0.09	4.24
1σ	0.61	0.01	0.21	0.02	0.01	0.01	0.04	0.21	0.09	0.01	0.00
RSCAS-20	75.76	0.10	13.97	0.60	0.06	0.08	0.65	3.64	5.15	0.12	4.19
1σ	0.27	0.01	0.07	0.03	0.00	0.01	0.03	0.10	0.06	0.01	0.23
RSCAS-21	75.51	0.08	15.86	0.50	0.07	0.05	1.56	2.15	4.22	0.82	10.61
1σ	0.46	0.01	0.54	0.04	0.02	0.01	0.15	0.22	0.08	0.17	0.71
RSCAS-22	77.43	0.08	13.57	0.58	0.05	0.05	1.41	2.32	4.50	0.83	10.02
1σ	0.52	0.01	0.19	0.03	0.01	0.01	0.07	0.21	0.13	0.12	0.52
RSCAS-23	73.52	0.09	15.22	0.65	0.06	0.08	0.81	3.86	5.70	0.23	4.63
1σ	0.33	0.01	0.08	0.03	0.00	0.01	0.03	0.09	0.05	0.01	0.15
RSCAS-24	76.58	0.09	14.01	0.60	0.06	0.07	0.72	2.84	5.03	0.25	7.01
1σ	0.25	0.01	0.06	0.03	0.01	0.01	0.04	0.04	0.09	0.01	0.29
RSCAS-25	78.93	0.08	13.02	0.55	0.06	0.07	0.78	1.85	4.66	0.35	9.38
1σ	0.36	0.02	0.13	0.02	0.01	0.01	0.02	0.07	0.06	0.02	0.42
RSCAS-26	78.20	0.08	13.19	0.58	0.06	0.07	0.97	2.24	4.62	0.74	8.70
1σ	0.29	0.01	0.12	0.03	0.00	0.01	0.05	0.08	0.12	0.04	0.42
Set-2 Experiments on andesite and water											
ASCAS-1	74.69	0.56	14.98	1.21	0.00	0.09	0.94	2.09	8.82	0.19	11.04
1σ	0.48	0.06	0.16	0.04	0.01	0.01	0.05	0.12	0.08	0.01	0.57
ASCAS-2	73.78	0.56	15.05	1.05	0.00	0.11	1.29	2.03	8.70	0.15	10.11
1σ	0.57	0.06	0.13	0.06	0.01	0.05	0.37	0.10	0.14	0.01	0.42
ASCAS-3	73.74	0.69	15.55	1.54	0.00	0.21	1.68	2.01	7.64	0.23	12.03
1σ	0.52	0.20	0.21	0.08	0.00	0.01	0.10	0.21	0.13	0.00	0.42
ASCAS-4	73.76	0.65	15.01	1.10	0.00	0.09	1.12	2.28	7.98	0.13	9.68
1σ	0.69	0.23	0.17	0.05	0.01	0.02	0.07	0.11	0.15	0.02	0.70
ASCAS-5	70.13	0.56	15.18	0.87	0.01	0.04	0.88	1.17	11.16	0.27	9.67
1σ	1.86	0.03	0.23	0.05	0.01	0.01	0.03	0.05	0.32	0.02	1.87
ASCAS-6	70.05	0.54	15.63	0.78	0.01	0.04	1.23	1.31	10.94	0.24	11.70
1σ	2.20	0.08	1.15	0.09	0.01	0.02	0.13	0.11	0.50	0.04	3.08

ASCAS-7	68.05	1.26	14.04	3.42	0.00	0.23	2.06	2.59	7.56	0.36	3.86
1σ	0.66	0.03	0.58	0.11	0.00	0.04	0.27	0.11	0.14	0.07	0.50
ASCAS-8	66.89	1.26	14.14	3.50	0.00	0.25	2.15	2.42	7.52	0.34	4.17
1σ	0.33	0.06	0.05	0.08	0.01	0.02	0.07	0.11	0.05	0.04	0.12
ASCAS-9	69.50	0.20	15.04	0.44	0.05	0.00	1.69	1.27	11.82	0.57	7.40
1σ	1.91	0.01	0.61	0.05	0.02	0.00	0.18	0.14	0.52	0.07	1.05
ASCAS-10	69.00	0.19	15.41	0.46	0.08	0.01	1.61	1.89	11.36	0.63	7.56
1σ	0.76	0.01	0.41	0.03	0.01	0.01	0.13	0.13	0.21	0.05	0.49
Set-3 Experiments on hydrous rhyolite at 1030 °C											
RSCAS-28	76.53	0.09	13.10	0.73	0.09	0.22	0.62	3.94	4.67	0.05	5.18
1σ	0.78	0.02	0.37	0.09	0.03	0.04	0.05	0.18	0.08	0.00	0.33
RSCAS-30	76.75	0.10	13.01	0.64	0.09	0.13	0.76	3.94	4.58	0.06	5.81
1σ	0.35	0.04	0.20	0.06	0.02	0.03	0.04	0.10	0.12	0.00	0.38
RSCAS-32	76.73	0.12	12.76	0.62	0.06	0.26	1.06	3.89	4.51	0.07	3.30
1σ	0.51	0.04	0.43	0.08	0.02	0.10	0.13	0.11	0.11	0.01	0.18
RSCAS-34	76.08	0.14	13.24	0.65	0.07	0.11	1.16	3.90	4.65	0.07	5.83
1σ	0.38	0.04	0.17	0.09	0.02	0.02	0.06	0.08	0.14	0.01	0.45
RSCAS-36	75.05	0.11	12.96	0.68	0.10	0.14	1.87	4.47	4.62	0.12	5.22
1σ	0.34	0.04	0.16	0.07	0.02	0.02	0.10	0.10	0.14	0.01	0.25
Set-4 Experiments on dry rhyolite at 1030 °C											
RSCAS-27	76.86	0.08	11.93	0.66	0.10	0.09	0.83	4.12	4.81	0.06	99.60
1σ	0.74	0.02	0.34	0.02	0.02	0.01	0.06	0.06	0.13	0.01	0.30
RSCAS-29	73.96	0.15	12.76	1.07	0.22	0.09	1.04	4.67	5.58	0.14	99.79
1σ	0.16	0.01	0.50	0.04	0.03	0.04	0.09	0.19	0.19	0.01	0.49
RSCAS-31	74.87	0.06	13.28	0.42	0.13	0.17	1.36	4.63	4.37	0.15	99.42
1σ	0.47	0.09	0.41	0.02	0.01	0.09	0.03	0.08	0.10	0.01	0.51
RSCAS-33	72.48	0.04	15.69	0.17	0.04	0.01	0.53	5.76	5.57	0.04	100.33
1σ	0.53	0.01	0.14	0.02	0.01	0.01	0.03	0.07	0.05	0.00	0.36
RSCAS-35	74.32	0.12	12.81	1.16	0.18	0.13	0.81	4.52	5.50	0.08	99.76
1σ	0.54	0.04	0.39	0.08	0.05	0.03	0.01	0.12	0.11	0.01	0.67

Major element contents are normalized to 100% on a dry basis except for the dry experiments of Set-4.
For each sample, typically 10–15 spots were analyzed, and 1σ is the standard deviation based on replicate analyses.

%), MgO (0.01–0.25 wt.%), FeO_t (0.4–3.5 wt.%), Na_2O (1.3–2.6 wt.%), and TiO_2 (0.2–1.3 wt.%). The large variation of these silicate melts in major element compositions was mainly caused by the different degrees of crystallization of clinopyroxene, rutile, and coesite. In the Set-3 and Set-4 experiments performed at a fixed temperature of 1030 °C (Table 2), the major element compositions of the silicate melts are nearly identical to those of the starting rhyolite, except for that the CaO content of the silicate melts increases by a factor of ~1–3.

The silicate melt water contents (4.2–11.3 wt.%) of six samples, as measured by FTIR, are consistent with those (4.2–11.8 wt.%) calculated based on the deficit of EPMA analytical totals from 100 wt.% (Fig. 4; Table 2). The water contents of these six samples well cover those of most of our samples (Table 2). Therefore, the silicate melt water contents for most of our hydrous samples were estimated using the EPMA-deficit approach, which range from 3.3 to 12.6 wt.% (Fig. 3f and Table 2). For the nominally dry experiments (the Set-4 experiments in Table 2), the EPMA totals are between 99.5 wt.% and 100.3 wt.%, and we assumed negligible amounts of water in the silicate melts.

3.3. The S concentration at anhydrite saturation in silicate melts

The SCAS in the silicate melts ranges from 170 to 3500 ppm. The SCSS in rhyolitic to rhyodacitic melts at 2–3 GPa and fO_2 below FMQ is ~50–150 ppm (Jégo and Dasgupta, 2013, 2014). Therefore, the contribution of S^{2-} to the measured SCAS in the two experiments saturated with pyrrhotite (RSCAS-13 and RSCAS-14) should be insignificant considering that the measured SCAS values of these two experiments are between 2700 and 3200 ppm. Fig. 5a shows that at 2–3 GPa, SCAS increases with increasing temperature for the experiments with 74–78 wt.% SiO_2 and 7.1–12.6 wt.% H_2O, in good agreement with previous results at low pressures (Masotta and Keppler, 2015; Zajacz and Tsay, 2019). A positive effect of water on SCAS was also observed in our study (Fig. 5b). For example, the silicate melts from runs RSCAS-19 and RSCAS-20 at 2 GPa and with 4.2 wt.% H_2O have SCAS values of 374–472 ppm; whereas, the silicate melts from runs RSCAS-21 and RSCAS-22 with 10.0–10.6 wt.% H_2O have SCAS values of ~3300 ppm at the same P–T conditions. SCAS also increases with increasing the CaO content of the silicate melt (Fig. 5c). This observation is consistent with previous results obtained at various pressures and temperatures for basaltic to rhyolitic melts (Chowdhury and Dasgupta, 2019). Fig. 5d shows that SCAS may also increase with increasing pressure. However, pressure is also correlated with the CaO and H_2O content of the silicate melts (Fig. 3c and f). Therefore, the observed correlation between pressure and SCAS could be ascribed to the correlation between pressure and the CaO and H_2O content of the silicate melt. The Set-3 and Set-4 experiments, which

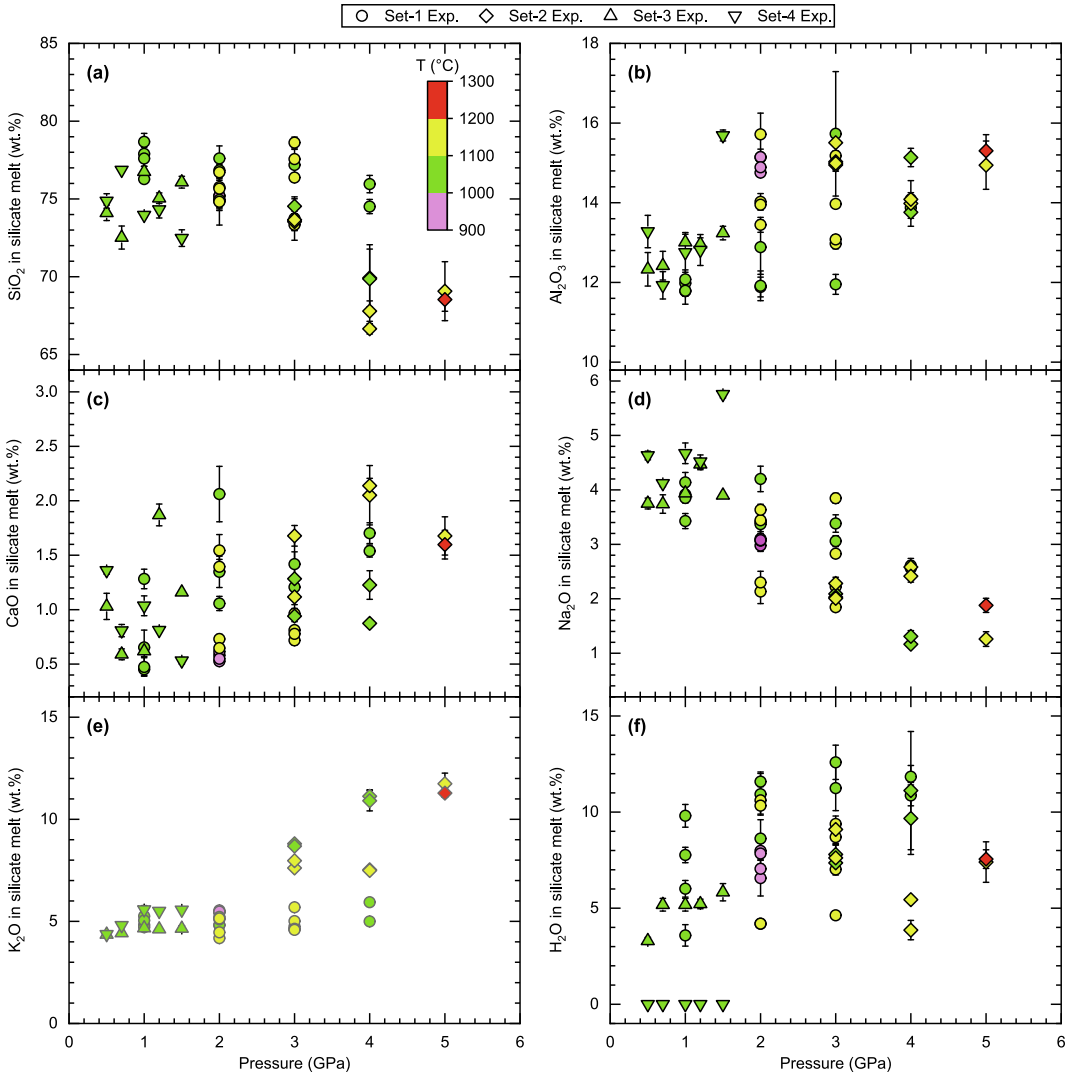

Fig. 3. Variation of major element composition of the produced silicate melts with experimental pressure. The plotted concentrations of all major elements were taken from Table 3, which were recalculated and normalized to 100% from EPMA results on a dry basis. The Set-1 experiments (Set-1 Exp.) started with rhyolite and water at 1–4 GPa and 900–1100 °C, the Set-2 experiments (Set-2 Exp.) started with andesite and water at 3–5 GPa and 1000–1200 °C, the Set-3 experiments (Set-3 Exp.) started with hydrous rhyolite with ~5 wt.% water at 0.5–1.5 GPa and 1030 °C, and the Set-4 experiments (Set-4 Exp.) started with dry rhyolite at 0.5–1.5 GPa and 1030 °C. See Table 2 for the detailed experimental conditions for all individual experiments.

have nearly constant melt composition and water content, were performed at 1030 °C and 0.5–1.5 GPa to independently evaluate the effect of pressure on SCAS. Fig. 5e and f show that SCAS is positively correlated with the CaO content of the silicate melt, rather than pressure. Accordingly, these experiments directly demonstrate that pressure does not considerably affect SCAS, which is in contrast to the studies of Li and Ripley (2009) and Baker and Moretti (2011) but consistent with the studies of Masotta and Keppler (2015), Chowdhury and Dasgupta (2019), and Zajacz and Tsay (2019).

3.4. Sample oxygen fugacity

In this study, runs RSCAS-13 and RSCAS-14 at 4 GPa are saturated with both pyrrhotite and anhydrite, and the other experiments are saturated with only anhydrite. Thus, the sample fO_2 should be higher than, or equivalent to, the fO_2 that stabilizes coexisting sulfide and sulfate phases in the silicate melts. Previous experiments show that at 2–3 GPa and 1050 °C, the fO_2 that stabilizes coexisting sulfide and anhydrite phases in rhyolitic to dacitic melts is ~FMQ+2 (Jégo and Dasgupta, 2014; Li et al., 2019). Accordingly, the fO_2 prevailing in our present experiments should be ≥FMQ+2. The presence of pyrrhotite in runs RSCAS-13 and RSCAS-14 at 4 GPa appears to be consistent with the studies of Jégo et al. (2016) and Matjuschkin et al. (2016), who proposed that the stability filed of sulfide may shift to high fO_2 with increasing pressure. However, pyrrhotite crystals were not found in our experiments at 5 GPa (the Set-2 experiments in Table 2).

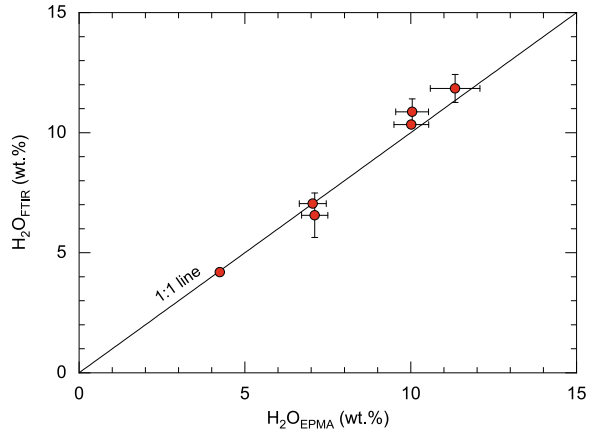

Fig. 4. Comparison of the water contents measured by FTIR and calculated by the deficit of EPMA totals from 100 wt.%. This figure shows that the FTIR and EPMA-deficit approaches yielded consistent water content in the silicate melt. Note that the water content in this plot ranged from 4.2 to 11.3 wt.%, covering the range of water content of most of our samples (Table 2).

4. DISCUSSION

4.1. Comparison with previous SCAS data

Previous experiments for measuring SCAS in silicate melts were done by Carroll and Rutherford (1987), Luhr (1990), Clemente et al. (2004), Costa et al. (2004), Jugo et al. (2005), Scaillet and MacDonald (2006), Beermann et al. (2011), Jégo and Pichavant (2012), Prouteau and Scaillet (2013), Jégo and Dasgupta (2014), Huang and Keppler (2015), Masotta and Keppler (2015), Chowdhury and Dasgupta (2019), and Zajacz and Tsay (2019). However, most of these experiments were conducted at pressures below 0.5 GPa for andesitic to rhyolitic melts. Jugo et al. (2005) and Chowdhury and Dasgupta (2019) reported SCAS data for basaltic to rhyolitic melts with experiments conducted at 0.5–3 GPa and 1050–1325 °C. These previous studies found that SCAS varies from a few tens of ppm to a few ten thousand of ppm, which is a multiple function of temperature, silicate melt composition, and silicate melt water content. The SCAS values in basaltic melts at 1–3 GPa and 1200–1350 °C are 7900–18000 ppm (Jugo et al., 2005; Chowdhury and Dasgupta, 2019), whereas the SCAS values are 32–4600 ppm in andesitic to rhyolitic melts at 700–1200 °C and pressures $<$ 0.5 GPa (Carroll and Rutherford, 1987; Luhr, 1990; Clemente et al., 2004; Costa et al., 2004; Scaillet and MacDonald, 2006; Huang and Keppler, 2015; Masotta and Keppler, 2015; Zajacz and Tsay, 2019). The experiments in this study were conducted at conditions of 0.5–5 GPa and 900–1200 °C, which are more relevant for partial melting of the subducting slab, so an intuitive comparison between the present and previous SCAS data cannot be made. However, our observations that SCAS increases with increasing temperature and the CaO and water content of the silicate melt (Fig. 5a–c) are in good agreement with previous results obtained at low pressures. The SCAS values (700–1500 ppm) obtained by Jégo and Dasgupta (2014) for rhyolitic melts with 4.4–4.7 wt.% water and at 2–3 GPa and 950 °C are well within the range of the SCAS values (320–3500 ppm) obtained at 2–3 GPa and 900–1000 °C in this study. To quantitatively understand the factors that potentially affect SCAS, we below test the accuracy of all previous SCAS models using our new SCAS data.

4.2. Test the accuracy of previous SCAS models

The dissolution of anhydrite in the silicate melt can be described as:

$$CaSO_4\ (anhydrite) = CaO\ (silicate\ melt) + SO_3\ (silicate\ melt) \quad (3)$$

The equilibrium constant or solubility product constant K_{SP} of Eq. (3) can be written as:

$$K_{SP} = \frac{\alpha_{SO_3} \cdot \alpha_{CaO}}{\alpha_{CaSO_4}} \quad (4)$$

where α_{SO_3} and α_{SO_3} denote activity of SO_3 and CaO in the silicate melt, respectively, and α_{CaSO_4} denotes activity of anhydrite. Since anhydrite is saturated in all experiments, α_{CaSO_4} equals one. Using chemical thermodynamics, Eq. (4) can be further written as:

$$\ln K_{SP} = \ln(x_{SO_3} \cdot x_{CaO}) + \ln(\gamma_{CaO} \cdot \gamma_{CaO}) = -\Delta G^0/RT = -(\Delta H_r^0 - T\Delta S_r^0 + \int \Delta V dP)/RT \quad (5)$$

where x and γ denote mole fraction and activity coefficient, respectively, R is gas constant, T is temperature in K, and ΔG^0 is Gibbs free energy. If we define $K_{sp}^* = x_{SO_3} \cdot x_{CaO}$, Eq. (5) can be written as:

$$\ln(K_{sp}^*) = -\frac{\Delta H_r^0 - T\Delta S_r^0 + \int \Delta V dP}{RT} - \ln(\gamma_{SO_3} \cdot \gamma_{CaO}) \quad (6)$$

where ΔH_r^0 is enthalpy change, ΔS_r^0 is entropy change, and ΔV is volume change for the reaction of Eq. (3). Eq. (6) can be further written as:

$$\ln(K_{sp}^*) = \frac{-\Delta H_r^0}{RT} + \frac{-\Delta V \cdot P}{T} + \frac{\Delta S_r^0}{R} - \ln(\gamma_{SO_3} \cdot \gamma_{CaO}) \quad (7)$$

and

$$\ln(SCAS) = \frac{-\Delta H_r^0}{RT} + \frac{-\Delta V \cdot P}{T} + \frac{\Delta S_r^0}{R} - \ln(\gamma_{SO_3} \cdot \gamma_{CaO}) - \ln(x_{CaO}) + C \quad (8)$$

where C is a constant. Eq. (8) implies that $\ln(SCAS)$ should be a multiple function of $1/T$, pressure, the CaO content of the silicate melt (x_{CaO}), and γ_{SO_3} and γ_{CaO}. The γ_{SO_3} and γ_{CaO} should be a function of the silicate melt composition and temperature. The effect of pressure could be negligible if ΔV is significantly small. Eq. (8) forms the thermodynamical basis for the calibration of SCAS models to quantitatively understand the effects of temperature, pressure, silicate melt composition, and silicate melt water content on SCAS and to accurately predict SCAS in the silicate melts at various conditions.

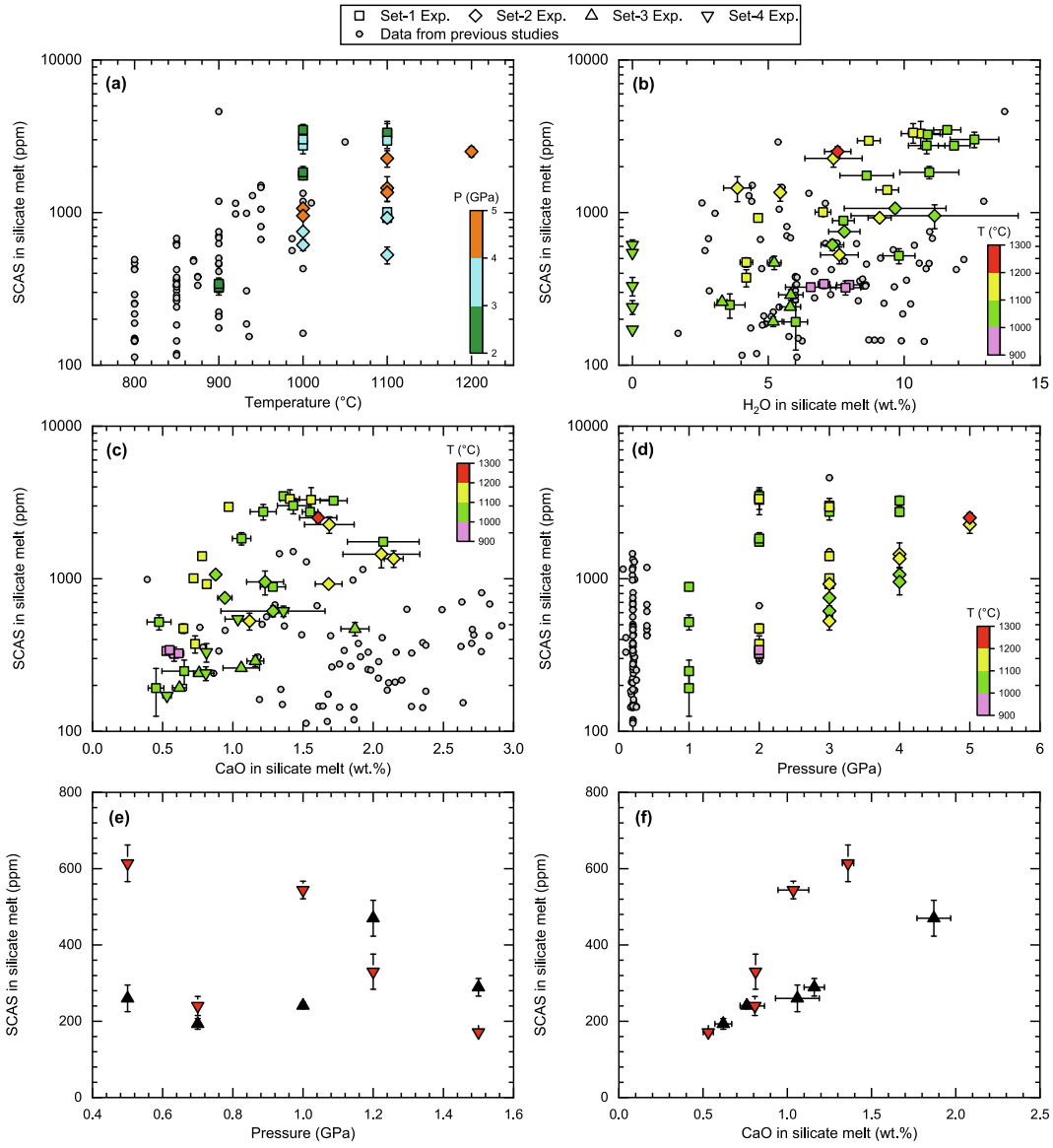

Fig. 5. Effects of pressure, temperature, silicate melt water content, and silicate melt CaO content on SCAS. The Set-1 to Set-4 experiments are the same as those shown in Fig. 3 (see also Table 2). In (a), the SCAS values from the Set-1 experiments with 7.1–12.6 wt.% water at 2–3 GPa, and the SCAS values from the Set-2 experiments, were selected to show the effect of temperature. In (b) and (c), all experimental data were plotted to show the general positive effect of the CaO and water content in the silicate melt on SCAS. In (d), the SCAS values from the Set-1 experiments with 73–79 wt.% SiO_2 and 3.6–12.6 wt.% H_2O, and the SCAS values from the Set-2 experiments with 68–72 wt.% SiO_2 and 3.9–12.0 wt.% H_2O, were selected to try to understand the effect of pressure. In (e) and (f), the SCAS values from the Set-3 and Set-4 experiments were plotted to show the correlation of SCAS and the CaO content of the silicate melt but negligible effect of pressure on SCAS. Note that the observed general positive correlation between SCAS and pressure in (d) is caused by the general position correlation between pressure, the silicate melt composition, and the silicate melt water content (Fig. 3), rather than pressure itself. The literature SCAS values from the silicate melts that contained >60 wt.% SiO_2, ~1.7–13.7 wt.% H_2O, and >0.4 wt.% CaO at 0.2–3 GPa and 800–1150 °C were selected for comparison. A summary of previous experimental *P–T* conditions, silicate melt major element compositions, silicate melt water content, and SCAS values was given in Table S2.

Several SCAS models have been calibrated by Li and Ripley (2009), Baker and Moretti (2011), Masotta and Keppler (2015), Chowdhury and Dasgupta (2019), and Zajacz and Tsay (2019), using the experimental SCAS data they measured and/or collected from the literature. The most recent two SCAS models put forward by Chowdhury and Dasgupta (2019) and Zajacz and Tsay (2019) revealed that although each previous SCAS model can well capture the SCAS data that were used to calibrate the model, they have a limited capacity in predicting new SCAS data that were not included in the model calibration. For example, Chowdhury and Dasgupta (2019) show that both the Li and Ripley (2009) model and the Baker and Moretti (2011) model moderately to highly overestimate

the SCAS values obtained from their experiments, while the Masotta and Keppler (2015) model was developed only for intermediate to felsic magmas and therefore cannot work for the silicate melts with $SiO_2 < 55$ wt.%. In addition, both the Li and Ripley (2009) and Baker and Moretti (2011) models suggest a positive effect of pressure on SCAS, but the models of Masotta and Keppler (2015), Chowdhury and Dasgupta (2019), and Zajacz and Tsay (2019) suggest a negligible effect of pressure. Using our new large dataset of SCAS values and all available literature data, we here test the accuracy of all previous SCAS models (Fig. 6). Fig. 6a shows that the Li and Ripley (2009) model overestimates our SCAS values and the SCAS values of Jégo and Dasgupta (2014), Huang and Keppler (2015), Masotta and Keppler (2015), Chowdhury and Dasgupta (2019), and Zajacz and Tsay (2019). Fig. 6b shows that the Baker and Moretti (2011) model highly overestimates our SCAS values and the SCAS values of Prouteau and Scaillet (2013), Jégo and Dasgupta (2014), and Chowdhury and Dasgupta (2019). Fig. 6c shows that the Masotta and Keppler (2015) model also highly overestimates our SCAS values, although the SiO_2 contents of our silicate melts (67–79 wt.%) are very close to those of the silicate melts of Masotta and Keppler (2015). In addition, the Masotta and Keppler (2015) model underestimates the SCAS values of Beermann et al. (2011), Chowdhury and Dasgupta (2019), and Zajacz and Tsay (2019). The Chowdhury and Dasgupta (2019) model capture most of the literature SCAS values but underestimates our SCAS values and the SCAS values of Huang and Keppler (2015) (Fig. 6d). Only the Zajacz and Tsay (2019) model well capture our new SCAS values and all available literature SCAS values with a mean

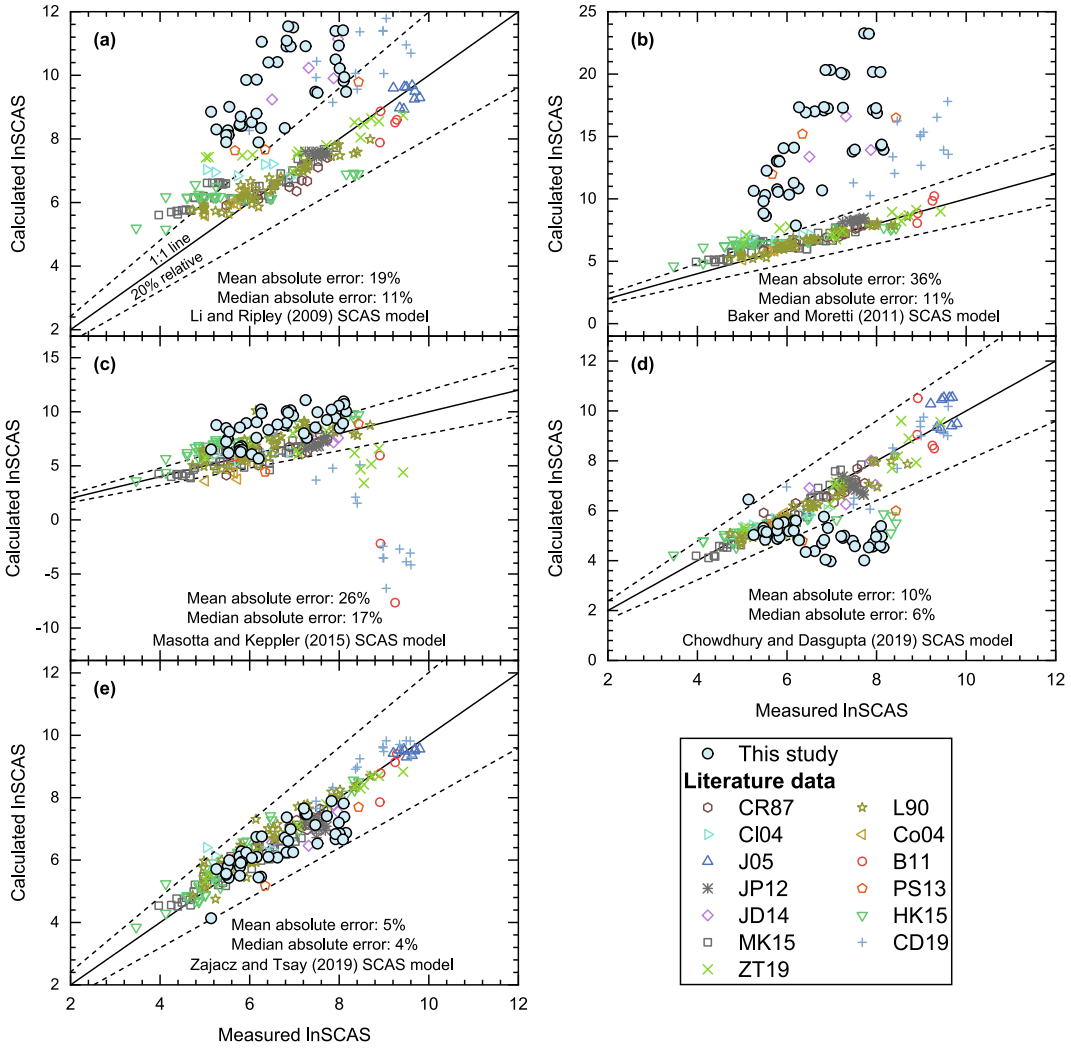

Fig. 6. Test the accuracy of all previous SCAS models using the new SCAS data in this study and all available literature SCAS data. The experimentally measured lnSCAS values were plotted against the predicted lnSCAS values using the SCAS models. This figure shows that only the Zajacz and Tsay (2019) model well captures all experimentally measured SCAS values with a great accuracy. The literature data were taken from CR87 (Carroll and Rutherford, 1987), L90 (Luhr, 1990), Cl04 (Clemente et al., 2004), Co04 (Costa et al., 2004), J05 (Jugo et al., 2005), B11 (Beermann et al., 2011), JP12 (Jégo and Pichavant, 2012), PS13 (Prouteau and Scaillet, 2013), JD14 (Jégo and Dasgupta, 2014), HK15 (Huang and Keppler, 2015), MK15 (Masotta and Keppler, 2015), CD19 (Chowdhury and Dasgupta, 2019), and ZT19 (Zajacz and Tsay, 2019).

and median absolute error of 5% and 4%, respectively (Fig. 6e), although the SCAS values of this study, Jégo and Pichavant (2012), Prouteau and Scaillet (2013), and Jégo and Dasgupta (2014) are not included in their model calibration. The success of the Zajacz and Tsay (2019) model in capturing our new SCAS data and the other SCAS data not included in the model calibration demonstrates its robustness in predicting SCAS in the silicate melts relevant for slab melting in subduction zones. The success of the Zajacz and Tsay (2019) model in capturing our new SCAS data also demonstrates an insignificant effect of pressure on SCAS, as discussed above, because the Zajacz and Tsay (2019) model does not include a pressure effect term of $\frac{-\Delta V \cdot P}{T}$. We thus strongly recommend the use of the Zajacz and Tsay (2019) model in predicting SCAS in the silicate melts at conditions relevant for subduction zones, as we will do in the following sections.

4.3. The SCAS in slab-derived silicate melts and the fate of S^{6+} during slab melting

To understand the cycle of S^{6+} during slab melting in subduction zones, we used the SCAS model of Zajacz and Tsay (2019) to predict the SCAS in slab-derived silicate melts. We took the slab surface P–T paths and sub-arc conditions from the D80 model of Syracuse et al. (2010). We bracketed the P–T segments of the subducting slab surface over which slab melting could occur, as done previously by Duncan and Dasgupta (2015). For slab sediment-derived silicate melts, we used the parameterization of Schmidt (2015) and Mann and Schmidt (2015) based on experimental results to estimate the major element compositions of the slab sediment-derived silicate melts as a function of pressure, temperature, and degree of partial melting. The water contents in the slab sediment-derived melts were varied from 3 to 10 wt.%, which well correspond to the water contents in the sediment-derived silicate melts produced experimentally at 3–5 GPa using a bulk water content of 0.7–1.5 wt.%. To predict the SCAS in slab sediment-derived silicate melts in a diapir, we assumed a melting temperature of 1100 °C according to Behn et al. (2011). The H_2O content in the sediment diapir was set to be 1–1.5 wt.%, which yielded ~2–4 wt.% water in the sediment-derived silicate melts at 3–5 GPa (Mann and Schmidt, 2015). To predict SCAS in partial melts of AOC, we used the major element compositions of partial melts that were produced experimentally from hydrous MORB-like compositions at P–T conditions most relevant for the subducting slab (Rapp and Watson 1995; Schmidt et al., 2004; Kessel et al., 2005; Jégo and Dasgupta, 2013, 2014).

The predicted SCAS values for slab sediment- and AOC-derived rhyolitic melts are presented in Fig. 7. Fig. 7a shows the predicted SCAS values for sediment-derived silicate melts at P–T conditions along the subducting slabs of Peru and Mexico. The predicted SCAS values range from 140 to 560 ppm, increasing with increasing slab P–T and the water content of the slab-derived silicate melts. The SCAS values of the Mexico slab-derived silicate melts are higher than those of the Peru slab-derived silicate melts by a factor of ~1.1–2.1 at a given pressure, due to the higher slab geothermal of Mexico. The SCAS values for the sediment diapir-derived silicate melts range from 810 to 1200 ppm due to the high melting temperature. Fig. 7b shows the predicted SCAS values for slab AOC-derived silicate melts, which range from ~520 to 6600 ppm and are strongly controlled by temperature. However, the SCAS values for slab AOC-derived silicate melts at P–T conditions along the subducting slab surface geothermal (P = 3–4 GPa; T = 850–1000 °C) are only ~540–1200 ppm but still higher than the SCAS values predicted for the slab sediment-derived silicate melts. This can be ascribed to the higher CaO content of the slab AOC-derived silicate melts than in the slab sediment-derived silicate melts at P–T conditions close to the subducting slab surface geothermal (Schmidt et al., 2004; Jégo and Dasgupta, 2013). Fig. 7c shows the predicted SCAS values for slab sediment-derived silicate melts of thirty subduction zones at the slab surface P–T conditions at the sub-arc depth where the solidus of hydrous sediment is crossed. The predicted SCAS values range from 80 to 390 ppm. The SCAS values predicted by fixing 3 wt.% and 10 wt.% water in the slab sediment-derived silicate melts are also plotted for comparison. The predicted SCAS values increase with increasing the melting temperature and pressure (P_{subarc}) and the water content of the slab sediment-derived melts.

Using the predicted SCAS values for slab-derived silicate melts, we can evaluate the fate of anhydrite during slab melting. The slab AOC and sediments may contain 1000–2000 ppm S (Alt and Shanks, 2011; Li and Schoonmaker, 2014). The fraction of S^{6+} in the subducting slab at 3–5 GPa remains unknown, but the fraction of S^{2-} must be significantly larger than that of S^{6+}, because the fO_2 of the subducting slab may decrease with increasing pressure as extensively discussed by Foley (2011) and Jégo and Dasgupta (2014). We tentatively assume 50–300 ppm S present as anhydrite in the subducting slab. In Fig. 7d, we compare our predicted SCAS values for the slab-derived silicate melts with the calculated S^{6+} contents of the slab-derived silicate melts assuming a perfect incompatibility of S^{6+} during slab melting. It can be seen from Fig. 7d that during slab melting of Peru subduction zone, anhydrite is saturated in the subducting slab if the slab contains no less than 50 ppm S^{6+}. If the S^{6+} content in the slab is no less than 200 ppm, slab partial melting would occur at anhydrite saturation for nearly all subduction zones. For partial melting at anhydrite saturation, the S^{6+} contents of the slab-derived silicate melts would equal the predicted SCAS. In the case of sediment-diapir melting, even if the sediments contain 300 ppm S^{6+}, anhydrite would still be exhausted due to the high degrees of partial melting and high SCAS in the silicate melts.

The results presented above indicate that slab-derived silicate melts globally cannot dissolve more than 1200 ppm S^{6+}, and the slab sediments-derived silicate melts even cannot dissolve more than 400 ppm S^{6+}. Assuming a S^{6+} content of 200 ppm in the AOC/sediment, the proportion of S^{6+} remaining in the slab after partial melting can be calculated using the predicted SCAS values and the calculated degrees of partial melting. For slab AOC-derived sil-

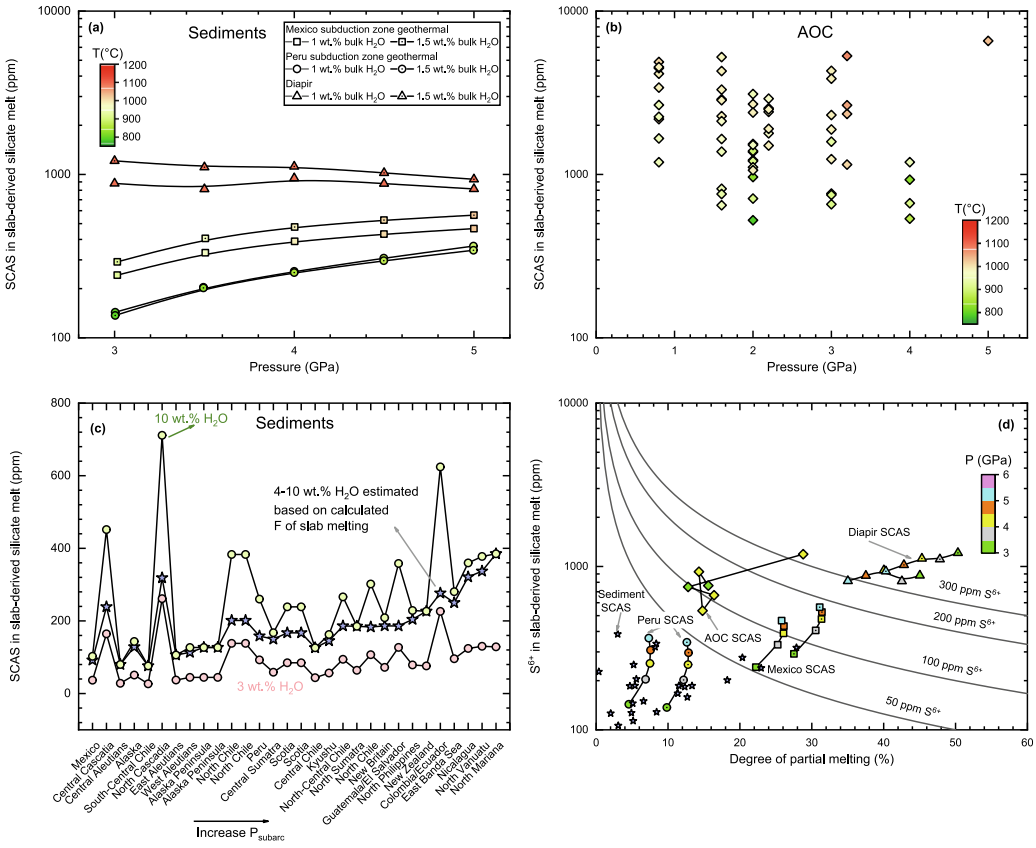

Fig. 7. Predicted SCAS or S^{6+} content in slab AOC- and sediment-derived silicate melts of global subduction zones. (a) The predicted SCAS for sediment-derived silicate melts along the geothermal of Mexico and Peru subduction zones and at *P–T* conditions of partial melting of the sediment diapir. The *P-T* conditions and the major element compositions of sediment-derived silicate melts are given in Table S3. (b) The predicted SCAS for AOC-derived silicate melts at various *P–T* conditions. The *P-T* conditions and the major element compositions of AOC-derived silicate melts are given in Table S4. (c) The predicted SCAS for sediment-derived silicate melts produced at the sub-arc depth in thirty subduction zones. A water content of 3–10 wt.% was assumed in the slab-derived silicate melts. (d) The S^{6+} content in slab-derived silicate melts as a function of degree of partial melting. The curves represent the S^{6+} content in slab-derived silicate melts assuming 50–300 ppm S^{6+} in the slab and perfectly incompatible behavior of S^{6+} during slab melting. The predicted SCAS values for silicate melts produced by partial melting of AOC or sediments with 1.5 wt.% H_2O at *P–T* conditions along the slab geothermal of Mexico and Peru subduction zones and at the sub-arc *P–T* conditions of global subduction zones were plotted. The results show that if the slab contains <200 ppm S^{6+}, anhydrite would be saturated during partial melting of most of the subduction zones because of the low SCAS in the slab-derived silicate melts. Slab *P–T* of Mexico and Peru subduction zones and slab *P–T* at the sub-arc depth for the other subduction zones in (c) were taken from the D80 model in Syracuse et al. (2010) and listed in Table S5. See text for more details.

icate melts with degree of partial melting and SCAS equivalent to 15% and 700 ppm, respectively (Fig. 7d), ~50% of the slab AOC S^{6+} would remain as anhydrite after extraction of the silicate melts. However, for slab sediment-derived silicate melts with degree of partial melting and SCAS equivalent to 10% and 300 ppm, respectively (Fig. 7d), ~85% of the slab sediment S^{6+} would remain as anhydrite after extraction of the silicate melts. We thus propose that slab-derived silicate melts have a considerable role in transferring slab S^{6+} to the sub-arc mantle; however, for most of the subduction zones, more than 70% of the anhydrite in slab sediments could survive hydrous partial melting at the sub-arc conditions, due to the low SCAS in the slab sediment-derived silicate melts (<400 ppm) (Fig. 7c, d). As suggested by Jégo and Dasgupta (2014), deep subduction of the anhydrite-bearing slab could in part account for the large deep subduction efficiency of the S in subduction zones (Li et al., 2020). The mantle plume-related oceanic island basalts may have sourced such anhydrite-bearing slab stored in the deep mantle, as evidenced by their high concentrations of S^{6+} (Moussallam et al., 2019).

With knowing the SCAS in slab-derived silicate melts, we can evaluate the effect of adding slab-derived silicate melts on the S abundance in the sub-arc mantle. We calculated the mass of S^{6+} brought by the slab-derived silicate melts to the sub-arc mantle using 200–1000 ppm S^{6+} in the slab-derived melts. Assuming the depleted sub-arc mantle has a S^{2-} abundance of 150 ppm (Saal et al., 2002), Fig. 8a shows the sub-arc mantle S abundance as a function of the proportion of slab-derived silicate melts added into the sub-arc mantle. It can be seen from Fig. 8a that to obtain the estimated S abundance of 200–500 ppm in the metasomatized sub-arc mantle (Métrich et al., 1999; de Hoog et al., 2001a), the required proportions of slab-

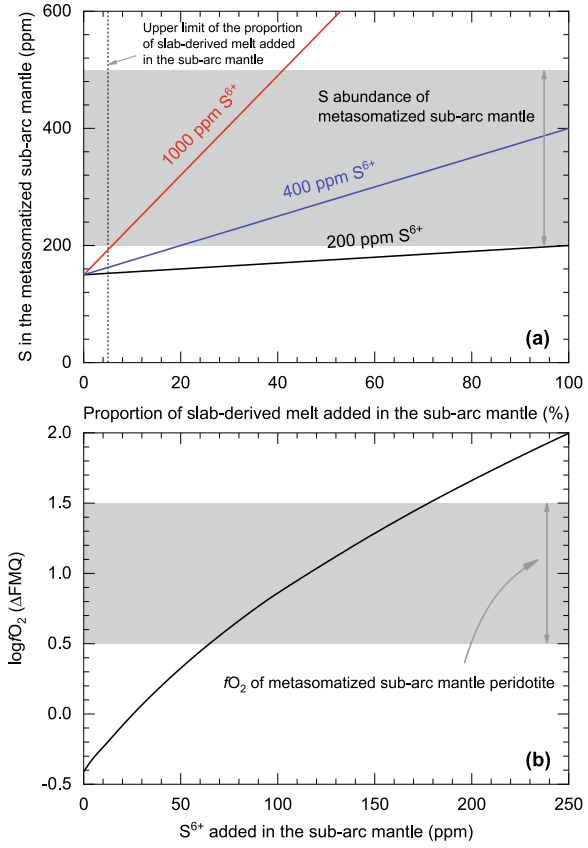

Fig. 8. (a) The S abundance of the metasomatized sub-arc mantle as a function of the proportion of slab-derived silicate melts added. The slab-derived silicate melts were assumed to contain 200–1000 ppm S^{6+}. Proportion of slab-derived silicate melts in the mantle source of arc magmas was estimated to be less than 5% based on the trace element and isotopic compositions of arc magmas (Singer et al., 2007; Mullen and McCallum, 2014), as indicated by the dashed line. The estimated S abundance in the metasomatized sub-arc mantle (200–500 ppm; Métrich et al.,1999; de Hoog et al., 2001a) was plotted for comparison. (b) The fO_2 of the metasomatized sub-arc mantle as a function of the mass of S^{6+} added. The range of measured fO_2 values for the metasomatized sub-arc mantle peridotites (FMQ+0.5 to FMQ+1.5; Parkinson and Arculus, 1999; Mallmann and O'Neill, 2007) was plotted for comparison. In (a), it demonstrates that the addition of slab-derived silicate melts cannot explain the estimated S abundance in the metasomatized sub-arc mantle. In (b), it demonstrates that the addition of slab S^{6+} can cause oxidization of the sub-arc mantle to fO_2 values consistent with the measured fO_2 values for the metasomatized sub-arc mantle peridotites.

derived silicate melts are ~6–100%, which are significantly higher than those (≤5%) constrained using trace elements and isotopes of arc magmas (Singer et al., 2007; Mullen and McCallum, 2014). Therefore, slab-derived silicate melts cannot contribute sufficient S^{6+} to fully explain the estimated S abundance in the metasomatized sub-arc mantle. Slab-derived fluids, which have a much larger capacity in dissolving both sulfide and sulfate species (Jégo and Dasgupta, 2013, 2014; Li et al., 2020), are accordingly required to transfer additional S from the slab to the sub-arc mantle to fully explain the estimated S abundance (200–500 ppm) in the metasomatized sub-arc mantle.

4.4. Implications for oxidation state of the metasomatized sub-arc mantle

Arc basalts are more oxidized than MORBs, as evidenced by their higher $Fe^{3+}/\Sigma Fe$ ratios (Kelley and Cottrell 2009, 2012; Brounce et al., 2014, 2015; Berry et al., 2018). However, as introduced previously, whether the oxidized nature of arc basalts is inherited from the sub-arc mantle or is derived from magmatic differentiation occurring in the lithosphere remains debated (Kelley and Cottrell, 2009, 2012; Evans et al. 2012; Grocke et al. 2016; Brounce et al., 2014, 2015; Lee et al., 2005, 2010, 2012; Li, 2018; Bénard et al., 2018; Tang et al., 2018; Feng and Li, 2019). Slab-derived and S^{6+}-bearing fluids/melts have been extensively proposed to oxidize and metasomatize the sub-arc mantle, and then partial melting of which produces the oxidized arc basalts (Mungall, 2002; Kelley and Cottrell, 2009; Evans, 2012; Kelley and Cottrell 2012; Brounce et al., 2014, 2015; Debret et al., 2016, 2020; Pons et al., 2016; Bénard et al., 2018; Walters et al., 2020). The measured high fO_2 values (FMQ+0.5 to FMQ+1.5) for the metasomatized sub-arc mantle peridotites (Parkinson and Arculus, 1999; Mallmann and O'Neill, 2007; Birner et al., 2017; Bénard et al., 2018) support this argument (McInnes et al., 2001; Bénard et al., 2018). The positive correlations between the degree of hydrous metasomatism of the sub-arc mantle, arc basalt water and S content, and arc basalt $Fe^{3+}/\Sigma Fe$ ratios and fO_2 values are also consistent with this argument (Kelley and Cottrell, 2009; Rowe et al., 2009; Zimmer et al., 2010; Brounce et al., 2014, 2015). In contrast, the V–Sc, Fe–Zn, V–Ga, and Cu–Re systematics of primitive MORBs and arc basalts imply that the metasomatized sub-arc mantle and the oceanic mantle may have similar oxidation state (Lee et al., 2005, 2010; Mallmann and O'Neill, 2009; Li, 2018), or the fO_2 of the metasomatized sub-arc mantle cannot be 0.5–1 log units higher than that of the oceanic mantle (Lee et al., 2012; Feng and Li, 2019). Wang et al. (2019) recently proposed that the temperature-dependent partitioning of V and Sc coupled with the relatively lower temperatures of arc basalts compared to MORBs indicates the sub-arc mantle one log unit more oxidized than the oceanic mantle. However, to parameterize the mineral/melt partition coefficients of V, Wang et al. (2019) implicitly assumed that V^{3+}, V^{4+}, and V^{5+} have an identical partitioning behavior as temperature and pressure vary, the validity of which is not demonstrated. Li (2018) actually showed that the partition coefficient ratios of V and Sc between clinopyroxene and silicate met are a constant value for the experiments performed in graphite capsules at 1050–1470 °C, indicating that varying temperature cannot cause V–Sc fractionations. As suggested by Li (2018), using the V–Sc systematics of primitive basalts to constrain mantle fO_2 remains valid until it independently demonstrates that varying temperature/pressure can cause V–Sc fractionations in basalts at fO_2 above the FMQ buffer.

Here we show that S^{6+} is a strong oxidizer during sub-arc mantle metasomatism but S^{2-} is a reducer during sub-arc mantle melting, and it is possible to use the S geochemistry to resolve the apparent paradox in the sub-arc mantle fO_2 as measured for the metasomatized sub-arc mantle peridotites and as inferred from the V–Sc, Fe–Zn, V–Ga, and Cu–Re systematics of primitive arc basalts. We consider the effect of adding slab-derived and S^{6+}-bearing melts/fluids on the $Fe^{3+}/\Sigma Fe$ of the sub-arc mantle according to a redox reaction as below:

$$S^{6+}\ (\text{slab-derived melt/fluid}) + 8Fe^{2+}\ (\text{silicate mineral}) = S^{2-}(sulfide) + 8Fe^{3+}(silicatemineral) \quad (9)$$

Eq. (9) indicates that metasomatism of the sub-arc mantle by S^{6+}-bearing melts/fluids would cause oxidation of the sub-arc mantle and production of sulfides. The redox reaction of Eq. (9) in the sub-arc mantle has been proposed in a few studies (Mungall, 2002; Evans, 2012; Bénard et al., 2018) and confirmed by both experimental and petrographic observations on metasomatized sub-arc mantle peridotites (McInnes et al., 2001; Birner et al., 2017; Bataleva et al., 2018). For example, the reaction of olivine with S^{6+}-bearing melts/fluids in the sub-arc mantle would produce Fe^{3+}-rich mineral assemblages of spinel, orthopyroxene, and/or clinopyroxene, with S^{6+} in the melts/fluids reduced as sulfides (McInnes et al., 2001; Bénard et al., 2018). Using Eq. (9) and pMELTS (Ghiorso et al., 2002), as has been done previously (Parkinson and Arculus, 1999; Evans, 2012), the sub-arc mantle fO_2 was calculated as a function of the mass of S^{6+} added to the sub-arc mantle at 2 GPa and 1000 °C (Fig. 8b). Fig. 8b shows that the addition of 65–250 ppm S^{6+} would enhance the sub-arc mantle fO_2 to a range of FMQ+0.5 to FMQ+2. These results confirm previous arguments that the addition of slab S^{6+} would cause oxidation of the sub-arc mantle (Kelley and Cottrell, 2009, 2012; Evans, 2012; Brounce et al., 2014, 2015; Birner et al., 2017). These results are also consistent with the measured fO_2 values (FMQ+0.5 to FMQ+1.5) for the metasomatized sub-arc mantle peridotites (Parkinson and Arculus, 1999; McInnes et al., 2001; Mallmann and O'Neill, 2007; Bénard et al., 2018). Therefore, the relatively higher fO_2 of the metasomatized sub-arc peridotites, compared to the oceanic mantle, can be explained by the addition of slab S^{6+} to the sub-arc mantle. However, does this mean that the primitive arc basalts produced by partial melting of the metasomatized sub-arc mantle have fO_2 values significantly higher than those of MORBs?

We below propose that Fe^{3+} is reduced by S^{2-} of sulfides during partial melting of the metasomatized sub-arc mantle, and the fO_2 values of primitive arc basalts are no higher than FMQ+0.5 to FMQ+1. We assume that partial melting of the metasomatized sub-arc mantle initiates at FMQ+1.5, which corresponds to ~180 ppm S^{6+} added in the sub-arc mantle during metasomatism. At fO_2 of FMQ+1.5, the S species in the basaltic melt is predominantly S^{6+} (Nash et al., 2019). However, because S is present as sulfides in the metasomatized sub-arc mantle as discussed above, a reaction involving the redox couples of S^{2-}–S^{6+} and Fe^{2+}–Fe^{3+} (similar to Eq. (9)) must occur and shift right during partial melting and sulfide dissolution in the produced basaltic melts:

$$S^{2-}\ (\text{sulfide/basaltic melt}) + 8Fe^{3+}\ (basalticmelt/silicatemineral) = S^{6+}(basalticmelt) + 8Fe^{2+}(basalticmelt/silicatemineral) \quad (10)$$

As a consequent, the fO_2 of the produced arc basalts, as well as the fO_2 of the sub-arc mantle, expressed as $Fe^{3+}/\Sigma Fe$, must decrease as partial melting of the metasomatized sub-arc proceeds, because more Fe^{3+} is reduced into Fe^{2+} by S^{2-} of sulfides with the degree of partial melting. However, the fO_2 would not decrease infinitively, because the $S^{6+}/\Sigma S$ in basalts is a function of both fO_2 and temperature (Nash et al., 2019). In addition, when the produced arc basalts are in equilibrium with the sub-arc mantle residuals at given P–T conditions, the arc basalt fO_2 corresponding to the Fe^{3+}–Fe^{2+} equilibria must equal the fO_2 corresponding to the S^{6+}–S^{2-} equilibria. The correlation between silicate melt Fe^{3+}/Fe^{2+}, fO_2, temperature, pressure, and silicate melt composition was given by Kress and Carmichael (1991):

$$\begin{aligned}\ln\left(\frac{Fe_2O_3}{FeO}\right) = {} & 0.196\cdot\ln f_{O_2} + \frac{1.1492\times10^4}{T} - 6.675 \\ & - 2.243\cdot x^{Al_2O_3} - 1.828\cdot x^{FeO_t} + 3.201 \\ & \cdot x^{CaO} + 5.854\cdot x^{Na_2O} + 6.215\cdot x^{K_2O} \\ & - 3.36\cdot\left[1 - \frac{1673}{T} - \ln\left(\frac{T}{1673}\right)\right] \\ & - 701\cdot\frac{P}{T} - 0.154\cdot\frac{(T-1673)\cdot P}{T} \\ & + 38.5\cdot\frac{P^2}{T}\end{aligned} \quad (11)$$

The correlation between basaltic melt S^{6+}/S^{2-}, Fe^{3+}/Fe^{2+}, and temperature was given by Nash et al. (2019):

$$\log\left(\frac{S^{6+}}{S^{2-}}\right) = 8\cdot\log\left(\frac{Fe^{3+}}{Fe^{2+}}\right) + \frac{8.7436\times10^6}{T^2} - \frac{27703}{T} + 20.273 \quad (12)$$

In Eqs. (11) and (12), T is temperature in K, P is pressure in GPa, and x^i refers to the mole fraction of an i oxide in the silicate melt. Using Eqs. (11) and (12), we have calculated the fO_2 of primitive arc basalts as a function of degree of partial melting of the metasomatized sub-arc mantle with an initial fO_2 of FMQ+1.5 (Fig. 9). For doing this, we assumed that partial melting of the sub-arc mantle occurs at 1.5–2 GPa, the major element compositions of the sub-arc mantle are similar to those of the depleted mantle (Workman and Hart, 2005), and the metasomatized sub-arc mantle contains 0.2–0.8 wt.% water according to the observed water content in arc basalts (Plank et al., 2013). We used pMELTS to calculate the major element compositions of primitive arc basalts and the melting temperature (1100–1450 °C) as a function of the degree of partial melting (F = 0–20%). The Fe_2O_3 content of the primitive arc basalts was constrained by the partitioning of Fe_2O_3 between mantle minerals and basaltic melt, and the used bulk partition coefficients are 0.25 according to recent experimental measurements (Sorbadere et al., 2018). The

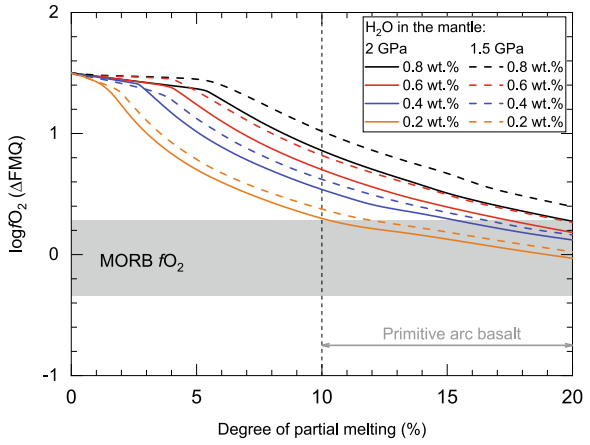

Fig. 9. The fO_2 of primitive arc basalts as a function of the degree of partial melting of the metasomatized sub-arc mantle at 1.5–2 GPa. Depleted mantle with different water contents was used as the mantle source of primitive arc basalts, and the major element compositions of the primitive arc basalts were calculated using pMELTS (Ghiorso et al., 2002). Marked melting degrees of the metasomatized sub-arc mantle for producing primitive arc magmas are 10–20% (Johnson et al., 2009; Portnyagin et al., 2007; Sadofsky et al., 2008; Kelley et al., 2010; Ruscitto et al., 2010; Plank et al., 2013). The metasomatized sub-arc mantle fO_2 before partial melting is FMQ+1.5. The fO_2 of MORBs (FMQ-0.34 to FMQ +0.28; Cottrell and Kelley, 2011; Zhang et al., 2018; Berry et al., 2018; Gaborieau et al., 2020) was plotted for comparison. See text for details of the calculations.

S^{2-} content of the sulfide-saturated basaltic melt was calculated using the SCSS model of Smythe et al. (2017). At a given degree of partial melting, when the reaction of Eq. (10) in basaltic melt and the partitioning of Fe_2O_3 between basaltic melt and mantle minerals reach equilibrium, the fO_2 of the primitive arc basalts was calculated using Eq. (11). Note that if Eq. (10) were not considered, the fO_2 of the produced arc basalts would not be considerably different from that of the metasomatized sub-arc mantle at a given pressure (Parkinson and Arculus, 1999). Also note that at a given degree of partial melting, the S^{6+}/S^{2-} in the primitive arc basalts, and the Fe^{3+}/Fe^{2+} in the primitive arc basalts and residual mantle minerals, were calculated iteratively using Eqs. (11) and (12) and the partitioning of Fe_2O_3 between basaltic melt and mantle minerals. Fig. 9 shows the calculated results, and a set of calculated results obtained at 2 GPa and 0.8 wt.% water in the metasomatized sub-arc mantle was presented in Table S6, which serves as a reference to reproduce our model. Fig. 9 illustrates that the fO_2 of primitive arc basalts decreases with the degree of partial melting, and a high water content in the primitive arc basalts corresponds to a high fO_2 value at a given degree of partial melting. The primitive arc basalts produced by small degrees of partial melting ($F < 6\%$) have fO_2 values above FMQ+1. However, when F equals 10–20%, at which conditions the primitive arc basalts are generated in most of the subduction zones (Johnson et al., 2009; Portnyagin et al., 2007; Sadofsky et al., 2008; Kelley et al., 2010; Ruscitto et al., 2010; Plank et al., 2013), the fO_2 values of the primitive arc basalts are no higher than FMQ+0.5 to FMQ+1 and approach the fO_2 values of MORBs. These fO_2 values are well consistent with those inferred for the metasomatized sub-arc mantle using the V–Sc, Fe–Zn, V–Ga, and Cu–Re systematics of primitive arc basalts. In addition, the S concentrations in the primitive arc basalts range from 1500 to 2800 ppm when the degree of partial melting equals 10–20%, with ~30–40% S present as S^{6+}. These S concentrations are well comparable to the observed S concentrations in arc basaltic melt inclusions hosted in olivine crystals (Wallace, 2005; Zimmer et al., 2010; Wallace and Edmonds, 2011; Kelley and Cottrell, 2012; Vigouroux et al., 2012; Brounce et al., 2014).

The following conclusions can be drawn from the above results. (1) The addition of slab-derived S^{6+} can oxidize the sub-arc mantle to fO_2 values of FMQ+0.5 to FMQ+1.5, as observed for the metasomatized sub-arc mantle peridotites. (2) During partial melting of the metasomatized sub-arc mantle, S^{2-} reduces Fe^{3+}, and the fO_2 values of primitive arc basalts are below FMQ+0.5 to FMQ+1. (3) The V–Sc, Fe–Zn, V–Ga, and Cu–Re systematics of primitive arc basalts thus record the fO_2 during partial melting of the metasomatized sub-arc mantle, rather than the fO_2 of the metasomatized sub-arc mantle. Arc basalts may thus become oxidized (with $fO_2 >$ FMQ+1) during magmatic differentiation, for example, by losing hydrogen and/or garnet crystallization in the lithospheric mantle (Tang et al., 2018; Tollan and Hermann, 2019; Tassara et al., 2020). (4) Although the fO_2 values of primitive arc basalts are no higher than FMQ+0.5 to FMQ+1, primitive arc basalts can still contain more than 1500 ppm S, similar to those observed for arc basalts (Wallace, 2005; Zimmer et al., 2010; Wallace and Edmonds, 2011; Kelley and Cottrell, 2012; Vigouroux et al., 2012; Brounce et al., 2014).

4.5. Fate of S^{6+} during arc magmatic differentiation and implications for the formation of Earth's continental crust

Although the fO_2 values of primitive arc basalts are no higher than FMQ+0.5 to FMQ+1 (Fig. 9), the $S^{6+}/\Sigma S$ ratios of primitive arc basalts are ~0.3–0.4. Oxidization of the evolving arc basalts to fO_2 values of up to FMQ+1.5 in the lithospheric mantle (Tang et al., 2018; Tollan and Hermann, 2019; Tassara et al., 2020) would convert more S^{2-} into S^{6+}, with $S^{6+}/\Sigma S$ above 0.8 in oxidized arc basalts (Nash et al., 2019). Therefore, the fate of S^{6+} during arc magmatic differentiation plays an important part in the S cycle in subduction zones. The formation of Earth's continental crust was ultimately associated with magmas at arcs with thickened crust (Lee et al., 2007; Rudnick and Gao, 2014; Tang et al., 2019; Chen et al., 2020; Li et al., 2021). However, Earth's continental crust contains ~400 ppm S (Rudnick and Gao, 2014), only approximately one fourth of the S concentration in oxidized arc basalts (Wallace, 2005; Wallace and Edmonds, 2011). The depletion of S in Earth's continental crust may imply that a significant amount of S was lost in sulfides during arc magmatic differentiation, which was then delaminated into the convecting mantle (Lee et al., 2012). However, the fate of S^{6+} during arc magmatic differentiation and its implications for the S

abundance in Earth's continental crust were not considered in previous studies.

The fate of S^{6+} during arc magmatic differentiation is controlled by a few factors, including SCAS in the silicate melt, the fluid/melt partitioning of S^{6+} when a fluid phase occurs, and the fO_2 of arc magmas (Li and Ripley, 2009; Masotta and Keppler, 2015; Masotta et al., 2016; Chowdhury and Dasgupta, 2019; Zajacz and Tsay, 2019). We here aim to model the fate of S^{6+} during arc magmatic differentiation and discuss its implications for the formation of Earth's continental crust. We took the average primitive basalt in the continental arc (Kelemen et al., 2014) as the parental arc basalt to differentiate. We assumed that the parental arc basalt contains 4 wt.% H_2O (Plank et al., 2013) and 3000 ppm CO_2 (Wallace, 2005; Shinohara, 2013). We considered arc magmatic differentiation occurs first in a magma chamber at the root of the thickened crust and then at the middle depth of the thickened crust (Annen et al., 2006), and the corresponding differentiation pressures were fixed at 1 GPa and 0.4 GPa, respectively. The fO_2 of the parental arc basalt was varied from FMQ+0.5 to FMQ+1.5 to investigate the effect of fO_2. The S concentration in the parental arc basalt was assumed to be 2000–3000 ppm, corresponding to the observed high end-members of the S concentrations in arc basaltic melt inclusions hosted in olivine crystals (Wallace, 2005; Zimmer et al., 2010; Wallace and Edmonds, 2011; Kelley and Cottrell, 2012; Vigouroux et al., 2012). The $S^{6+}/\Sigma S$ ratio in the parental arc basalt at fO_2 between FMQ+0.5 and FMQ+1.5 was calculated using Eq. (12) and a liquidus temperature of 1250 °C for the parental arc basalt. The major element composition and the CO_2 and H_2O content of the residual silicate melt, and the modal abundances of minerals produced during each step of near-fractional crystallization were calculated using Rhyolite-MELTS (Ghiorso and Gualda, 2015). The Fe^{3+}/Fe^{2+} ratio in the parental arc basalt was calculated according to the assumed fO_2 using Eq. (11), and the Fe^{3+}/Fe^{2+} ratio in the differentiating magma was calculated using mineral/silicate melt partition coefficients of Fe^{3+} and Fe^{2+} reported in Mallmann and O'Neill (2009). When the differentiating arc magma is saturated with a fluid phase, degassing occurs following an open system degassing scenario, and both S^{6+} and S^{2-} partition between the fluid phase and the silicate melt. In our model, a fluid phase occurs only in andesitic and more felsic magmas at 0.4 GPa (see below). We used the fluid/melt partition coefficients of S^{6+} ($D_{S^{6+}}^{fluid/melt}$) taken from Zajacz and Tsay (2019) who parameterized $D_{S^{6+}}^{fluid/melt}$ as a function of silicate melt NBO/T at 0.2 GPa. The effects of temperature and the 0.2 GPa pressure difference between this study and Zajacz and Tsay (2019) on $D_{S^{6+}}^{fluid/melt}$ are thought to be negligible in our model (Masotta et al., 2016). The fluid/melt partition coefficients of S^{2-} ($D_{S^{2-}}^{fluid/melt}$) are a strong function of temperature and silicate melt composition; decreasing temperature decreases $D_{S^{2-}}^{fluid/melt}$, but more felsic melts have higher $D_{S^{2-}}^{fluid/melt}$ (Scaillet and MacDonald, 2006; Keppler, 2010; Jégo and Dasgupta, 2013). Therefore, the effects of temperature and silicate melt composition on $D_{S^{2-}}^{fluid/melt}$ are cancelled out for a differentiating magma. In our model, we used $D_{S^{2-}}^{fluid/melt}$ values of 100–300 to cover the potential variation of $D_{S^{2-}}^{fluid/melt}$ during arc magmatic differentiation at 0.4 GPa.

The effect of S degassing on the fO_2 of the differentiating arc magma was considered because the redox couples of S^{2-}–S^{6+} and Fe^{2+}–Fe^{3+} are involved in the degassing process (Métrich et al., 2009; Wallace and Edmonds, 2011; Kelley and Cottrell, 2012; Moussallam et al., 2016). The dominant S species in volcanic gasses is SO_2 (Wallace, 2005; Métrich et al., 2009; Oppenheimer et al., 2011); however, H_2S could be an important S species at pressures of several kbar even at fO_2 above FMQ (Gaillard and Scaillet, 2009; Binder and Keppler, 2011). The degassing of both SO_2 and H_2S from an oxidized magma, in which S dissolves as sulfate S^{6+}, would cause oxidation of the residual magma but to a different extent:

$$S^{6+}\ (\text{melt}) + 2Fe^{2+}\ (\text{melt}) + 2O^{2-}\ (\text{melt}) = 2Fe^{3+}(melt) + SO_2(fluid) \quad (13)$$

$$S^{6+}\ (\text{melt}) + 8Fe^{2+}\ (\text{melt}) + 2H^{+}\ (\text{melt}) = 8Fe^{3+}(melt) + H_2S(fluid) \quad (14)$$

In contrast, the degassing of H_2S for a reduced magma, in which S dissolves as sulfide S^{2-}, would not change the oxidation of the residual magma, but the degassing of SO_2 would cause reduction of the residual magma:

$$S^{2-}\ (\text{melt}) + 6Fe^{3+}\ (\text{melt}) + 2O^{2-}\ (\text{melt}) = 6Fe^{2+}(melt) + SO_2(fluid) \quad (15)$$

A strong reduction of the oxidation state of basaltic magmas by S degassing was observed by Kelley and Cottrell (2012) and Moussallam et al. (2016), but S degassing does not necessarily cause the change of oxidation state of a magma (Brounce et al., 2014). Therefore, to understand the effect of S degassing on the Fe^{3+}/Fe^{2+} ratio in the differentiating arc magma at 0.4 GPa, we calculated the SO_2/H_2S ratios in the fluid phase using the gas–melt equilibrium models of Gaillard and Scaillet (2009), Gaillard et al. (2011), and Burgisser et al. (2015). In addition, the SCSS and SCAS in the silicate melt of the differentiating arc magma were calculated using the Smythe et al. (2017) model and the Zajacz and Tsay (2019) model, respectively. When the S^{2-} and/or S^{6+} concentration in the differentiating arc magma exceeds the corresponding SCSS and/or SCAS, sulfide and/or anhydrite saturate and segregate from the differentiating magma.

In each step of arc magmatic differentiation, we considered the interactions among sulfide, anhydrite, fluid, silicate mineral, and silicate melt in terms of the partitioning of Fe^{2+}, Fe^{3+}, S^{2-}, and S^{6+} and the redox equilibrium between Fe^{2+}–Fe^{3+} and S^{2-}–S^{6+} couples, using an iterative approach. The modeled results are shown in Fig. 10 as a function of the MgO content in the differentiating arc magma, with a set of results provided in Table S7 serving as a reference for reproducing our model. Fig. 10 shows that in the deep magma chamber, nearly all S is stored in the silicate melt at fO_2 between FMQ+1 and FMQ+1.5. However, at fO_2 between FMQ+0.5 and FMQ+1, sulfide

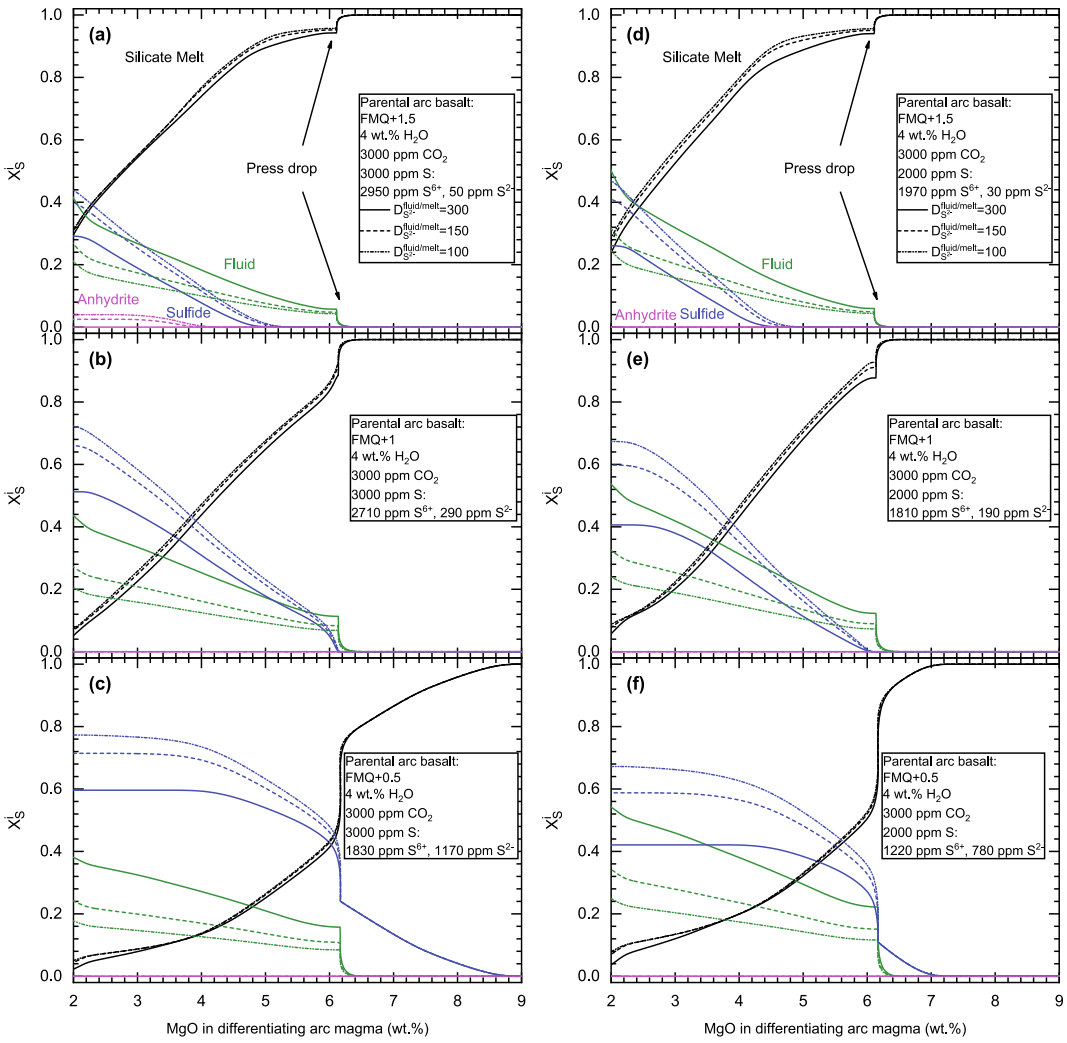

Fig. 10. The proportion of S (X_S^i) in silicate melt, anhydrate, sulfide, and fluid during arc magmatic differentiation from a hydrous parental basalt in a continental arc setting. The parental magma was assumed to contain 4 wt.% H_2O, 3000 ppm CO_2 and 3000 or 2000 ppm S, and $D_{S^{2-}}^{fluid/melt}$ values were 300, 150 and 100. The fO_2 of the parental arc basalt was varied from FMQ+0.5 to FMQ+1.5, and the total S^{6+} and S^{2-} contents in the parental arc basalt at a given fO_2 were calculated using Eq. (12). We assumed that arc magmatic differentiation takes place first in a deep magma chamber at 1 GPa and then in a shallow magma chamber at 0.4 GPa, as marked by the arrow for pressure drop. See text for more details of the calculations.

saturates and sequesters more than 20% of the total S in the parental arc basalt. A fluid phase does not occur in the deep magma chamber because of the high solubility of CO_2 and water in the silicate melt at high pressures (Mattey, 1991; Pan et al., 1991; Lesne et al., 2011; Botcharnikov et al., 2015; Eguchi and Dasgupta, 2017; Mitchell et al., 2017). During arc magmatic differentiation in the shallow magma chamber, a fluid phase occurs and up to 50% of the total S in the parental arc basalt partitions into the fluid phase at fO_2 between FMQ+0.5 and FMQ+1.5. Anhydrite occurs in the differentiating magma only at fO_2 of FMQ+1.5, but it does not sequester more than 5% of the total S in the parental arc basalt. At fO_2 between FMQ+0.5 and FMQ+1, up to 75% of the total S in the parental arc basalt is lost in sulfide. When the MgO content of the differentiating magma equals that of the bulk continental crust (~4.7 wt.%; Rudnick and Gao, 2014), about 20–60% of the total S in the parental arc basalt is stored in the silicate melt at fO_2 between FMQ+0.5 and FMQ+1, and ~60–90% of the total S in the parental arc basalt is stored in the silicate melt at fO_2 between FMQ+1 and FMQ+1.5. Fig. 11a and c show the variation of fO_2 as a function of the MgO content in the differentiating magma. The fO_2 of the differentiating magma is nearly constant or slightly increases with decreasing the MgO content in the deep magma chamber. However, in the shallow magma chamber, S degassing causes a substantial decrease in the fO_2 of the differentiating magma when the parental arc basalt is at fO_2 between FMQ+0.5 and FMQ+1. This is not the case for the fO_2 of the differentiating magma when the parental arc basalt is at fO_2 between FMQ+1 and FMQ+1.5, because significant fractions of S are present as S^{6+} in the silicate melt and degassing of which cannot lead to reduction of the differentiating magma. Fig. 11a and c also show comparisons

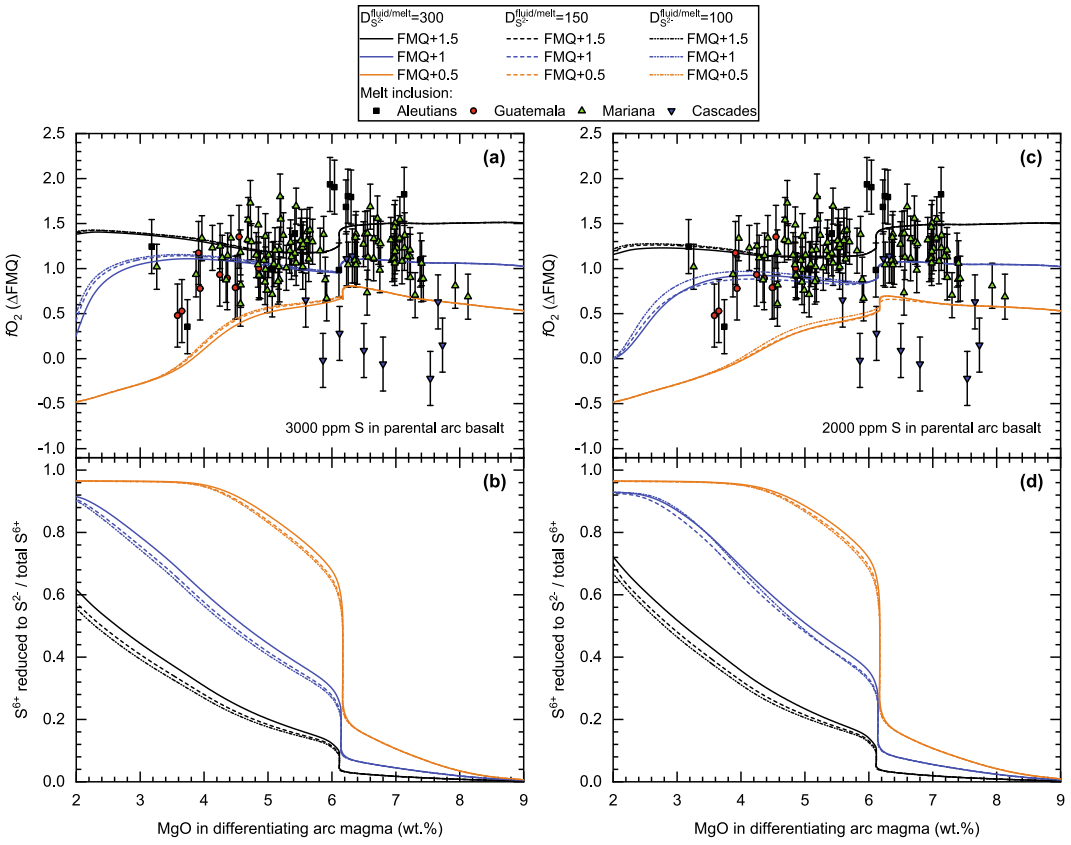

Fig. 11. (a, c) The fO_2 of arc magma differentiated from a hydrous parental basalt in the continental arc setting. The fO_2 of the parental arc basalt was varied from FMQ+0.5 to FMQ+1. The fO_2 values of some arc melt inclusion hosted in olivine crystals from Kelley and Cottrell (2009, 2012); Rowe et al. (2009); Zimmer et al. (2010); Lloyd et al. (2013); and Brounce et al. (2014) were plotted for comparisons. (b, d) The proportion of the total S^{6+} in the parental arc basalt reduced to S^{2-} during arc magmatic differentiation. The parental arc basalt was assumed to contain 4 wt.% H_2O, 3000 ppm CO_2 and 3000 or 2000 ppm S. See Fig. 10 and the main text for more details of the calculations.

between the modeled fO_2 values of the differentiating arc magma and the measured fO_2 values of natural arc magmas from Aleutians, Guatemala, and Mariana (Kelley and Cottrell, 2009, 2012; Zimmer et al., 2010; Lloyd et al., 2013; Brounce et al., 2014), which arcs have crustal thickness less than 20 km (Chiaradia, 2014). The fO_2 values of natural arc magmas from Cascades, with a crustal thickness larger than 30 km (Chiaradia, 2014), are below FMQ+1 (Rowe et al., 2009). Overall, the modeled fO_2 values cover those of the natural arc magmas; however, it should be noted that most of the studied arc magmas in thin arcs experienced degassing at pressures lower than the pressure modeled here (0.4 GPa). Fig. 11b and d show that during differentiation of the arc magma, a significant fraction of S^{6+} in the parental arc basalt is converted into S^{2-}. This is mainly because the decrease of magmatic temperature during differentiation causes the $S^{6+}/\Sigma S$ ratio in the silicate melt shifted to low values (Nash et al., 2019). Sulfide precipitation and S^{2-}-degassing further promote the conversion of S^{6+} into S^{2-} in the silicate melt. Mass-balance calculations show that 55–95% of the S^{6+} in the parental arc basalt is converted into S^{2-} during magmatic differentiation when the parental arc basalt is at fO_2 between FMQ+0.5 and FMQ+1.5 (Fig. 11b, d).

The above results can be used to understand the formation conditions of Earth's continental crust. The depletion of S in the continental crust, compared to the S concentrations in arc basalts, could apparently imply that a significant amount of arc magmatic S^{6+} was lost in anhydrite during arc magmatic differentiation, which was then delaminated into the convecting mantle during the formation of Earth's continental crust. However, the saturation of anhydrite usually occurs at the late stages of arc magmatic differentiation (Fig. 10a), which means that anhydrite occurs mainly in oxidized andesitic to rhyolitic magmas as observed in arc magmatic rocks (Parat et al., 2011). In addition, the rocks delaminated into the depleted mantle are usually mafic pyroxenite/gabbro accumulates (e.g., Lee et al., 2012; Chen et al., 2020). Therefore, the low S abundance in Earth's continental crust cannot be explained by the delamination of anhydrite-bearing mafic accumulates from Earth's continental crust root into the convecting mantle. Furthermore, if the parental arc basalt is at fO_2 between FMQ+1 and FMQ+1.5, the differentiating arc magma at ~4.7 wt.% MgO contains more than 1000 ppm S, which is twice that in Earth's continental crust. Therefore, Earth's continental crust may not have formed from parental arc basalts with fO_2 above FMQ+1. Fig. 10c

and f show if the parental arc basalt is at fO_2 of FMQ+0.5, a significant amount of sulfide forms during arc magmatic differentiation, and the arc magma at ~4.7 wt.% MgO contains ~400–600 ppm S, which are well comparable to the S abundance in Earth's continental crust. Thus, we safely conclude that if Earth's continental crust formed from arc basalts, the fO_2 of the arc basalts should not have been significantly higher than FMQ+0.5 to FMQ+1, and delamination of sulfide-bearing mafic accumulates into the convecting mantle (Lee et al., 2012) appears to be the only approach to obtain the estimated S abundance (~400 ppm) in Earth's continental crust (Rudnick and Gao, 2014). These conclusions are consistent with recent studies focusing on modeling the evolution of Cu and other chalcophile elements in global arc magmas, which also concluded that Earth's continental crust formed in continental arcs at fO_2 between FMQ and FMQ+1 (Lee et al., 2012; Chen et al., 2020; Li et al., 2021). It may be worth noting that the high fO_2 of the evolved thin arc magmas from Aleutians, Guatemala, and Mariana, as shown in Fig. 11a and c, does not mean Earth's continental crust formed from very oxidized arc magmas, which, rather, means that Earth's crust formed at arcs with thickened crust (>30 km), as constrained by the Nb, Ta, and chalcophile element abundance in global arc magmas and Earth's continental crust (Tang et al., 2019; Chen et al., 2020; Li et al., 2021).

5. CONCLUSIONS

Forty-three experiments were performed at 0.5–5 GPa and 900–1200 °C to measure SCAS in slab-derived rhyodacitic to rhyolitic melts, which varies from 170 to 3500 ppm as a multiple function of temperature, pressure, silicate melt composition, and silicate melt water content. We found SCAS increases with increasing temperature and the CaO and water content of the silicate melt, but the effect of pressure on SCAS is negligible. We used our new SCAS data and all available literature data ($n = 252$) to test the accuracy of all previous SCAS models calibrated for predicting SCAS in silicate melts at various conditions. The results show that the Zajacz and Tsay (2019) model works as the best SCAS model in capturing all SCAS data with a mean and median absolute error of 5% and 4%, respectively. We therefore strongly recommend the use of the Zajacz and Tsay (2019) SCAS model when predicting SCAS in silicate melts relevant for magmatism in subduction zones. The fate of S^{6+} during slab melting of global subduction zones was investigated, and we found that the slab-derived silicate melts can dissolve 130–1200 ppm S^{6+}, but it cannot contribute enough S to explain the estimated S abundance in the metasomatized sub-arc mantle. Thus, slab-derived fluids are required to bring additional S to fully explain the estimated S abundance in the metasomatized sub-arc mantle. The addition of slab S^{6+} can cause oxidation of the sub-arc mantle in an fO_2 range of FMQ +0.5 to FMQ+2, consistent with the fO_2 values measured for the metasomatized sub-arc mantle peridotites. However, during partial melting of the metasomatized sub-arc mantle, S^{2-} of sulfides is a reducer and the fO_2 of primitive arc basalts cannot be higher than FMQ+0.5 to FMQ+1, which is consistent with the sub-arc mantle fO_2 inferred from the Fe–Zn, V–Sc, V–Ga, and Cu–Re systematics of primitive arc basalts. The high fO_2 (>FMQ+1) of arc basalts is likely established during magmatic differentiation in the lithospheric mantle. Finally, the fate of S^{6+} during arc magmatic differentiation in a thickened continental arc setting was modeled to understand the formation conditions of Earth's continental crust. We found that significant fractions of S^{6+} in the parental arc basalts are converted into S^{2-} and lost in sulfides during arc magmatic differentiation. We then concluded that Earth's continental crust cannot have formed from arc basalts with fO_2 significantly higher than FMQ+0.5 to FMQ+1 to explain its estimated S abundance (400 ppm).

Declaration of Competing Interest

The authors declare that they have no known competing financial interests or personal relationships that could have appeared to influence the work reported in this paper.

ACKNOWLEDGMENTS

We thank Chang-Ming Xing, Wancai Li, and Haoran Dou for the assistance in EPMA measurements, Li Li, and Pan Qu for the assistance in FTIR and Raman measurements. This study received financial supports from National Key R&D Program of China (2018YFA0702702) and the National Natural Science Foundation of China (42021002) to Y.L. We would also like to thank Sébastien Jégo, Shuo Ding and an anonymous reviewer for their constructive comments, and Rajdeep Dasgupta for his constructive comments and editorial handling of the manuscript.

APPENDIX A. SUPPLEMENTARY MATERIAL

Supplementary data to this article can be found online at https://doi.org/10.1016/j.gca.2021.05.027.

REFERENCES

Alt J. C. (1995) Sulfur isotopic profile through the oceanic crust: Sulfur mobility and seawater-crustal sulfur exchange during hydrothermal alteration. *Geology* **23**, 585–588.

Alt J. C. and Shanks W. C. (2011) Microbial sulfate reduction and the sulfur budget for a complete section of altered oceanic basalts, IODP Hole 1256D (eastern Pacific). *Earth Planet. Sci. Lett.* **310**, 73–83.

Alt J. C., Shanks W. C. and Jackson M. C. (1993) Cycling of sulfur in subduction zones: The geochemistry of sulfur in the Mariana Island Arc and back-arc trough. *Earth Planet. Sci. Lett.* **119**, 477–494.

Alt J. C., Laverne C., Coggon R. M., Teagle D. A. H., Banerjee N. R., Morgan S., Smith-Duque C. E., Harris M. and Galli L. (2010) Subsurface structure of a submarine hydrothermal system in ocean crust formed at the East Pacific Rise, ODP/IODP Site 1256. *Geochem. Geophys. Geosyst.* **11**, Q10010.

Annen C., Blundy J. D. and Sparks R. S. J. (2006) The Genesis of Intermediate and Silicic Magmas in Deep Crustal Hot Zones. *J. Petrol.* **47**, 505–539.

Audétat A. and Simon A. (2012) Magmatic controls on porphyry copper deposits. *Soc. Econ. Geol. Spec. Pub.* **16**, 573–618.

Baker D. R. and Moretti R. (2011) Modeling the Solubility of Sulfur in Magmas: A 50-Year Old Geochemical Challenge. *Rev. Mineral. Geochem.* **73**, 167–213.

Bataleva Y., Palyanov Y. and Borzdov Y. (2018) Sulfide Formation as a Result of Sulfate Subduction into Silicate Mantle (Experimental Modeling under High P, T-Parameters). *Minerals-Basel* **8**, 373.

Beermann O., Botcharnikov R. E., Holtz F., Diedrich O. and Nowak M. (2011) Temperature dependence of sulfide and sulfate solubility in olivine-saturated basaltic magmas. *Geochim. Cosmochim. Acta* **75**, 7612–7631.

Behn M. D., Kelemen P. B., Hirth G., Hacker B. R. and Massonne H.-J. (2011) Diapirs as the source of the sediment signature in arc lavas. *Nat. Geosci.* **4**, 641–646.

Bénard A., Klimm K., Woodland A. B., Arculus R. J., Wilke M., Botcharnikov R. E., Shimizu N., Nebel O., Rivard C. and Ionov D. A. (2018) Oxidising agents in sub-arc mantle melts link slab devolatilisation and arc magmas. *Nat. Commun.* **9**, 3500.

Berry A. J., Stewart G. A., O'Neill H. S. C., Mallmann G. and Mosselmans J. F. W. (2018) A re-assessment of the oxidation state of iron in MORB glasses. *Earth Planet. Sci. Lett.* **483**, 114–123.

Binder B. and Keppler H. (2011) The oxidation state of sulfur in magmatic fluids. *Earth Planet. Sci. Lett.* **301**, 190–198.

Birner S. K., Warren J. M., Cottrell E., Davis F. A., Kelley K. A. and Falloon T. J. (2017) Forearc Peridotites from Tonga Record Heterogeneous Oxidation of the Mantle following Subduction Initiation. *J. Petrol.* **58**, 1755–1780.

Botcharnikov R. E., Holtz F. and Behrens H. (2015) Solubility and fluid–melt partitioning of H_2O and Cl in andesitic magmas as a function of pressure between 50 and 500MPa. *Chem. Geol.* **418**, 117–131.

Botcharnikov R. E., Linnen R. L., Wilke M., Holtz F., Jugo P. J. and Berndt J. (2011) High gold concentrations in sulphide-bearing magma under oxidizing conditions. *Nat. Geosci.* **4**, 112–115.

Brounce M. N., Kelley K. A. and Cottrell E. (2014) Variations in $Fe^{3+}/\sum Fe$ of Mariana Arc Basalts and Mantle Wedge fO_2. *J. Petrol.* **55**, 2513–2536.

Brounce M., Kelley K. A., Cottrell E. and Reagan M. K. (2015) Temporal evolution of mantle wedge oxygen fugacity during subduction initiation. *Geology* **43**, 775–778.

Burgisser A., Alletti M. and Scaillet B. (2015) Simulating the behavior of volatiles belonging to the C-O–H–S system in silicate melts under magmatic conditions with the software D-Compress. *Comput. Geosci.* **79**, 1–14.

Carroll M. R. and Rutherford M. J. (1987) The Stability of Igneous Anhydrite: Experimental Results and Implications for Sulfur Behavior in the 1982 El Chichon Trachyandesite and Other Evolved Magmas. *J. Petrol.* **28**, 781–801.

Chang J. and Audétat A. (2018) Petrogenesis and Metal Content of Hornblende-Rich Xenoliths from Two Laramide-age Magma Systems in Southwestern USA: Insights into the Metal Budget of Arc Magmas. *J. Petrol.* **59**, 1869–1898.

Chen K., Tang M., Lee C.-T.-A., Wang Z., Zou Z., Hu Z. and Liu Y. (2020) Sulfide-bearing cumulates in deep continental arcs: The missing copper reservoir. *Earth Planet. Sci. Lett.* **531**, 115971.

Chiaradia M. (2014) Copper enrichment in arc magmas controlled by overriding plate thickness. *Nature Geosci.* **7**, 43–46.

Chowdhury P. and Dasgupta R. (2019) Effect of sulfate on the basaltic liquidus and Sulfur Concentration at Anhydrite Saturation (SCAS) of hydrous basalts – Implications for sulfur cycle in subduction zones. *Chem. Geol.* **522**, 162–174.

Clemente B., Scaillet B. and Pichavant M. (2004) The solubility of sulphur in hydrous rhyolitic melts. *J. Petrol.* **45**, 2171–2196.

Costa F., Scaillet B. and Pichavant M. (2004) Petrological and Experimental Constraints on the Pre-eruption Conditions of Holocene Dacite from Volcán San Pedro (36°S, Chilean Andes) and the Importance of Sulphur in Silicic Subduction-related Magmas. *J. Petrol.* **45**, 855–881.

Cooper L. B., Ruscitto D. M., Plank T., Wallace P. J., Syracuse E. M. and Manning C. E. (2012) Global variations in H_2O/Ce: 1. Slab surface temperatures beneath volcanic arcs. *Geochem. Geophys. Geosyst.* **13**, Q03024.

Cottrell E. and Kelley K. A. (2011) The oxidation state of Fe in MORB glasses and the oxygen fugacity of the upper mantle. *Earth Planet. Sci. Lett.* **305**, 270–282.

Dasgupta R. (2013) Ingassing, Storage, and Outgassing of Terrestrial Carbon through Geologic Time. *Rev. Mineral. Geochem.* **75**, 183–229.

Debret B., Millet M.-A., Pons M.-L., Bouilhol P., Inglis E. and Williams H. (2016) Isotopic evidence for iron mobility during subduction. *Geology* **44**, 215–218.

Debret B., Reekie C. D. J., Mattielli N., Beunon H., Ménez B., Savov I. and Williams H. M. (2020) Redox transfer at subduction zones: insights from Fe isotopes in the Mariana forearc. *Geochem. Perspect. Lett.* **12**, 46–51.

Defant M. J. and Drummond M. S. (1990) Derivation of some modern arc magmas by melting of young subducted lithosphere. *Nature* **347**, 662–665.

de Hoog J. C. M., Mason P. R. D. and van Bergen M. J. (2001a) Sulfur and chalcophile elements in subduction zones: constraints from a laser ablation ICP-MS study of melt inclusions from Galunggung Volcano, Indonesia. *Geochim. Cosmochim. Acta* **65**, 3147–3164.

de Hoog J. C. M., Taylor B. E. and van Bergen M. J. (2001b) Sulfur isotope systematics of basaltic lavas from Indonesia: implications for the sulfur cycle in subduction zones. *Earth Planet. Sci. Lett.* **189**, 237–252.

Duncan M. S. and Dasgupta R. (2015) Pressure and temperature dependence of CO_2 solubility in hydrous rhyolitic melt: implications for carbon transfer to mantle source of volcanic arcs via partial melt of subducting crustal lithologies. *Contrib. Mineral. Petrol.* **169**, 54.

Eguchi J. and Dasgupta R. (2017) CO_2 content of andesitic melts at graphite-saturated upper mantle conditions with implications for redox state of oceanic basalt source regions and remobilization of reduced carbon from subducted eclogite. *Contrib. Mineral. Petrol.* **172**, 12.

Evans K. A. (2012) The redox budget of subduction zones. *Earth-Sci. Rev.* **113**, 11–32.

Evans K. A., Elburg M. A. and Kamenetsky V. S. (2012) Oxidation state of subarc mantle. *Geology* **40**, 783–786.

Feng L. u. and Li Y. (2019) Comparative partitioning of Re and Mo between sulfide phases and silicate melt and implications for the behavior of Re during magmatic processes. *Earth Planet. Sci. Lett.* **517**, 14–25.

Foley S. F. (2011) A Reappraisal of Redox Melting in the Earth's Mantle as a Function of Tectonic Setting and Time. *J. Petrol.* **52**, 1363–1391.

Gaborieau M., Laubier M., Bolfan-Casanova N., McCammon C. A., Vantelon D., Chumakov A. I., Schiavi F., Neuville D. R. and Venugopal S. (2020) Determination of $Fe^{3+}/\Sigma Fe$ of olivine-hosted melt inclusions using Mössbauer and XANES spectroscopy. *Chem. Geol.* **547**, 119646.

Gaillard F. and Scaillet B. (2009) The sulfur content of volcanic gases on Mars. *Earth Planet. Sci. Lett.* **279**, 34–43.

Gaillard F., Scaillet B. and Arndt N. T. (2011) Atmospheric oxygenation caused by a change in volcanic degassing pressure. *Nature* **478**, 229–232.

Ghiorso M. S., Hirschmann M. M., Reiners P. W. and Kress, III, V. C. (2002) The pMELTS: A revision of MELTS for improved calculation of phase relations and major element partitioning related to partial melting of the mantle to 3 GPa. *Geochem. Geophys. Geosyst.* **3**, 1030.

Ghiorso M. S. and Gualda G. A. R. (2015) An H_2O-CO_2 mixed fluid saturation model compatible with rhyolite-MELTS. *Contrib. Mineral. Petrol.* **169**, 53.

Grocke S. B., Cottrell E., de Silva S. and Kelley K. A. (2016) The role of crustal and eruptive processes versus source variations in controlling the oxidation state of iron in Central Andean magmas. *Earth Planet. Sci. Lett.* **440**, 92–104.

Grondahl C. and Zajacz Z. (2017) Magmatic controls on the genesis of porphyry Cu–Mo–Au deposits: The Bingham Canyon example. *Earth Planet. Sci. Lett.* **480**, 53–65.

Hermann J. and Spandler C. J. (2008) Sediment Melts at Sub-arc Depths: an Experimental Study. *J. Petrol.* **49**, 717–740.

Hilton D. R., Fischer T. P. and Marty B. (2002) Noble Gases and Volatile Recycling at Subduction Zones. *Rev. Mineral. Geochem.* **47**, 319–370.

Huang R. and Keppler H. (2015) Anhydrite stability and the effect of Ca on the behavior of sulfur in felsic magmas. *Am. Mineral.* **100**, 257–266.

Hutchinson M. C. and Dilles J. H. (2019) Evidence for Magmatic Anhydrite in Porphyry Copper Intrusions. *Econ. Geol.* **114**, 143–152.

Jégo S. and Pichavant M. (2012) Gold solubility in arc magmas: Experimental determination of the effect of sulfur at 1000°C and 0.4GPa. *Geochim. Cosmochim. Acta* **84**, 560–592.

Jégo S. and Dasgupta R. (2013) Fluid-present melting of sulfide-bearing ocean-crust: Experimental constraints on the transport of sulfur from subducting slab to mantle wedge. *Geochim. Cosmochim. Acta* **110**, 106–134.

Jégo S. and Dasgupta R. (2014) The Fate of Sulfur During Fluid-Present Melting of Subducting Basaltic Crust at Variable Oxygen Fugacity. *J. Petrol.* **55**, 1019–1050.

Jégo S., Nakamura M., Kimura J.-I., Iizuka Y., Chang Q. and Zellmer G. F. (2016) Is gold solubility subject to pressure variations in ascending arc magmas?. *Geochim. Cosmochim. Acta* **188**, 224–243.

Johnson M. C. and Plank T. (1999) Dehydration and melting experiments constrain the fate of subducted sediments. *Geochem. Geophys. Geosyst.* **1**, 1007.

Johnson E. R., Wallace P. J., Delgado Granados H., Manea V. C., Kent A. J. R., Bindeman I. N. and Donegan C. S. (2009) Subduction-related Volatile Recycling and Magma Generation beneath Central Mexico: Insights from Melt Inclusions, Oxygen Isotopes and Geodynamic Models. *J. Petrol.* **50**, 1729–1764.

Jugo P. J., Luth R. W. and Richards J. P. (2005) An Experimental Study of the Sulfur Content in Basaltic Melts Saturated with Immiscible Sulfide or Sulfate Liquids at 1300°C and 1.0 GPa. *J. Petrol.* **46**, 783–798.

Kagoshima T., Sano Y., Takahata N., Maruoka T., Fischer T. P. and Hattori K. (2015) Sulphur geodynamic cycle. *Sci. Rep.* **5**, 8330.

Kelemen P. B., Hanghøj K. and Greene A. R. (2014) One View of the Geochemistry of Subduction-Related Magmatic Arcs, with an Emphasis on Primitive Andesite and Lower Crust. In *Treatise on Geochemistry* (ed. K. K. Turekian), second ed. Elsevier, Oxford, pp. 749–806.

Kelley K. A. and Cottrell E. (2009) Water and the Oxidation State of Subduction Zone Magmas. *Science* **325**, 605–607.

Kelley K. A. and Cottrell E. (2012) The influence of magmatic differentiation on the oxidation state of Fe in a basaltic arc magma. *Earth Planet. Sci. Lett.* **329-330**, 109–121.

Kelley K. A., Plank T., Newman S., Stolper E. M., Grove T. L., Parman S. and Hauri E. H. (2010) Mantle Melting as a Function of Water Content beneath the Mariana Arc. *J. Petrol.* **51**, 1711–1738.

Keppler H. (2010) The distribution of sulfur between haplogranitic melts and aqueous fluids. *Geochim. Cosmochim. Acta* **74**, 645–660.

Kessel R., Ulmer P., Pettke T., Schmidt M. W. and Thompson A. B. (2005) The water–basalt system at 4 to 6 GPa: Phase relations and second critical endpoint in a K-free eclogite at 700 to 1400 °C. *Earth Planet. Sci. Lett.* **237**, 873–892.

Kress V. C. and Carmichael I. S. E. (1991) The compressibility of silicate liquids containing Fe_2O_3 and the effect of composition, temperature, oxygen fugacity and pressure on their redox states. *Contrib. Mineral. Petrol.* **108**, 82–92.

Lee C. T., Leeman W. P., Canil D. and Li Z. (2005) Similar V/Sc Systematics in MORB and Arc Basalts: Implications for the Oxygen Fugacities of their Mantle Source Regions. *J. Petrol.* **46**, 2313–2336.

Lee C.-T., Morton D. M., Kistler R. W. and Baird A. K. (2007) Petrology and tectonics of Phanerozoic continent formation: From island arcs to accretion and continental arc magmatism. *Earth Planet. Sci. Lett.* **263**, 370–387.

Lee C.-T., Luffi P., Le Roux V., Dasgupta R., Albaréde F. and Leeman W. P. (2010) The redox state of arc mantle using Zn/Fe systematics. *Nature* **468**, 681–685.

Lee C.-T., Luffi P., Chin E. J., Bouchet R., Dasgupta R., Morton D. M., Le Roux V., Yin Q.-Z. and Jin D. (2012) Copper Systematics in Arc Magmas and Implications for Crust-Mantle Differentiation. *Science* **336**, 64–68.

Lesne P., Scaillet B., Pichavant M., Iacono-Marziano G. and Beny J.-M. (2011) The H_2O solubility of alkali basaltic melts: an experimental study. *Contrib. Mineral. Petrol.* **162**, 133–151.

Li C. and Ripley E. M. (2009) Sulfur Contents at Sulfide-Liquid or Anhydrite Saturation in Silicate Melts: Empirical Equations and Example Applications. *Econ. Geol.* **104**, 405–412.

Li J.-L., Schwarzenbach E. M., John T., Ague J. J., Huang F., Gao J., Klemd R., Whitehouse M. J. and Wang X.-S. (2020) Uncovering and quantifying the subduction zone sulfur cycle from the slab perspective. *Nat. Commun.* **11**, 514.

Li Y. (2018) Temperature and pressure effects on the partitioning of V and Sc between clinopyroxene and silicate melt: Implications for mantle oxygen fugacity. *Am. Mineral.* **103**, 819–823.

Li Y., Feng L., Kiseeva E. S., Gao Z., Guo H., Du Z., Wang F. and Shi L. (2019) An essential role for sulfur in sulfide-silicate melt partitioning of gold and magmatic gold transport at subduction settings. *Earth Planet. Sci. Lett.* **528**, 115850.

Li Y., Audétat A., Liu Z. and Wang F. (2021) Chalcophile element partitioning between Cu-rich sulfide phases and silicate melt and implications for the formation of Earth's continental crust. *Geochim. Cosmochim. Acta* **302**, 61–82.

Li Y. H. and Schoonmaker J. E. (2014) Chemical Composition and Mineralogy of Marine Sediments. In *Treatise on Geochemistry* (eds. H. D. Holland and K. K. Turekian), second ed. Elsevier, Oxford, pp. 1–32.

Lloyd A. S., Plank T., Ruprecht P., Hauri E. H. and Rose W. (2013) Volatile loss from melt inclusions in pyroclasts of differing sizes. *Contrib. Mineral. Petrol.* **165**, 129–153.

Luhr J. F. (1990) Experimental Phase Relations of Water- and Sulfur-Saturated Arc Magmas and the 1982 Eruptions of El Chichón Volcano. *J. Petrol.* **31**, 1071–1114.

Mallmann G. and O'Neill H. S. C. (2007) The effect of oxygen fugacity on the partitioning of Re between crystals and silicate

melt during mantle melting. *Geochim. Cosmochim. Acta* **71**, 2837–2857.

Mallmann G. and O'Neill H. S. C. (2009) The Crystal/Melt Partitioning of V during Mantle Melting as a Function of Oxygen Fugacity Compared with some other Elements (Al, P, Ca, Sc, Ti, Cr, Fe, Ga, Y, Zr and Nb). *J. Petrol.* **50**, 1765–1794.

Mann U. and Schmidt M. W. (2015) Melting of pelitic sediments at subarc depths: 1. Flux vs. fluid-absent melting and a parameterization of melt productivity. *Chem. Geol.* **404**, 150–167.

Masotta M. and Keppler H. (2015) Anhydrite solubility in differentiated arc magmas. *Geochim. Cosmochim. Acta* **158**, 79–102.

Masotta M., Keppler H. and Chaudhari A. (2016) Fluid-melt partitioning of sulfur in differentiated arc magmas and the sulfur yield of explosive volcanic eruptions. *Geochim. Cosmochim. Acta* **176**, 26–43.

Matjuschkin V., Blundy J. D. and Brooker R. A. (2016) The effect of pressure on sulphur speciation in mid-to deep-crustal arc magmas and implications for the formation of porphyry copper deposits. *Contrib. Mineral. Petrol.* **171**, 66.

Mattey D. P. (1991) Carbon dioxide solubility and carbon isotope fractionation in basaltic melt. *Geochim. Cosmochim. Acta* **55**, 3467–3473.

McInnes B. I., Gregoireb M., Binnsa R. A., Herzigc P. M. and Hanningtond M. D. (2001) Hydrous metasomatism of oceanic sub-arc mantle, Lihir, Papua New Guinea: petrology and geochemistry of£ uid-metasomatised mantle wedge xenoliths. *Earth Planet. Sci. Lett.* **188**, 169–183.

Métrich N., Schiano P., Clocchiatti R. and Maury R. C. (1999) Transfer of sulfur in subduction settings: an example from Batan Island (Luzon volcanic arc, Philippines). *Earth Planet. Sci. Lett.* **167**, 1–14.

Métrich N., Berry A. J., O'Neill H. S. C. and Susini J. (2009) The oxidation state of sulfur in synthetic and natural glasses determined by X-ray absorption spectroscopy. *Geochim. Cosmochim. Acta* **73**, 2382–2399.

Mitchell A. L., Gaetani G. A., O'Leary J. A. and Hauri E. H. (2017) H_2O solubility in basalt at upper mantle conditions. *Contrib. Mineral. Petrol.* **172**, 85.

Moussallam Y., Edmonds M., Scaillet B., Peters N., Gennaro E., Sides I. and Oppenheimer C. (2016) The impact of degassing on the oxidation state of basaltic magmas: A case study of Kīlauea volcano. *Earth Planet. Sci. Lett.* **450**, 317–325.

Moussallam Y., Longpré M.-A., McCammon C., Gomez-Ulla A., Rose-Koga E. F., Scaillet B., Peters N., Gennaro E., Paris R. and Oppenheimer C. (2019) Mantle plumes are oxidised. *Earth Planet. Sci. Lett.* **527** 115798.

Mullen E. K. and McCallum I. S. (2014) Origin of Basalts in a Hot Subduction Setting: Petrological and Geochemical Insights from Mt. Baker. *J. Petrol.* **55**, 241–281.

Mungall J. E. (2002) Roasting the mantle: Slab melting and the genesis of major Au and Au-rich Cu deposits. *Geology* **30**, 915–918.

Nash W. M., Smythe D. J. and Wood B. J. (2019) Compositional and temperature effects on sulfur speciation and solubility in silicate melts. *Earth Planet. Sci. Lett.* **507**, 187–198.

Nichols G. T., Wyllie P. J. and Stern C. R. (1994) Subduction zone melting of pelagic sediments constrained by melting experiments. *Nature* **371**, 785–788.

Ohlhorst S., Behrens H. and Holtz F. (2001) Compositional dependence of molar absorptivities of near-infrared OH- and H_2O bands in rhyolitic to basaltic glasses. *Chem. Geol.* **174**, 5–20.

Oppenheimer C., Scaillet B. and Martin R. S. (2011) Sulfur Degassing From Volcanoes: Source Conditions, Surveillance, Plume Chemistry and Earth System Impacts. *Rev. Mineral. Geochem.* **73**, 363–421.

Pan V., Holloway J. R. and Hervig R. L. (1991) The pressure and temperature dependence of carbon dioxide solubility in tholeiitic basalt melts. *Geochim. Cosmochim. Acta* **55**, 1587–1595.

Parat F., Holtz F. and Streck M. J. (2011) Sulfur-bearing Magmatic Accessory Minerals. *Rev. Mineral. Geochem.* **73**, 285–314.

Parkinson I. J. and Arculus R. J. (1999) The redox state of subduction zones: insights from arc-peridotites. *Chem. Geol.* **160**, 409–423.

Pertermann M. and Hirschmann M. M. (2003) Anhydrous Partial Melting Experiments on MORB-like Eclogite: Phase Relations, Phase Compositions and Mineral-Melt Partitioning of Major Elements at 2–3 GPa. *J. Petrol.* **44**, 2173–2201.

Plank T., Kelley K. A., Zimmer M. M., Hauri E. H. and Wallace P. J. (2013) Why do mafic arc magmas contain ~4wt% water on average? *Earth Planet Sci. Lett.* **364**, 168–179.

Pons M.-L., Debret B., Bouilhol P., Delacour A. and Williams H. (2016) Zinc isotope evidence for sulfate-rich fluid transfer across subduction zones. *Nat. Commun.* **7**, 13794.

Portnyagin M., Hoernle K., Plechov P., Mironov N. and Khubunaya S. (2007) Constraints on mantle melting and composition and nature of slab components in volcanic arcs from volatiles (H_2O, S, Cl, F) and trace elements in melt inclusions from the Kamchatka Arc. *Earth Planet. Sci. Lett.* **255**, 53–69.

Prouteau G. and Scaillet B. (2013) Experimental Constraints on Sulphur Behaviour in Subduction Zones: Implications for TTG and Adakite Production and the Global Sulphur Cycle since the Archean. *J. Petrol.* **54**, 183–213.

Rapp R. P. and Watson E. B. (1995) Dehydration Melting of Metabasalt at 8–32 kbar: Implications for Continental Growth and Crust-Mantle Recycling. *J. Petrol.* **36**, 891–931.

Rowe M. C., Kent A. J. R. and Nielsen R. L. (2009) Subduction Influence on Oxygen Fugacity and Trace and Volatile Elements in Basalts Across the Cascade Volcanic Arc. *J. Petrol.* **50**, 61–91.

Rudnick R. L. and Gao S. (2014) Composition of the Continental Crust. In *Treatise on Geochemistry* (eds. H. D. Holland and K. K. Turekian), second ed. Elsevier, Oxford, pp. 1–51.

Ruscitto D. M., Wallace P. J., Johnson E. R., Kent A. J. R. and Bindeman I. N. (2010) Volatile contents of mafic magmas from cinder cones in the Central Oregon High Cascades: Implications for magma formation and mantle conditions in a hot arc. *Earth Planet. Sci. Lett.* **298**, 153–161.

Saal A. E., Hauri E. H., Langmuir C. H. and Perfit M. R. (2002) Vapour undersaturation in primitive mid-ocean-ridge basalt and the volatile content of Earth's upper mantle. *Nature* **419**, 451–455.

Sadofsky S. J., Portnyagin M., Hoernle K. and van den Bogaard P. (2008) Subduction cycling of volatiles and trace elements through the Central American volcanic arc: evidence from melt inclusions. *Contrib. Mineral. Petrol.* **155**, 433–456.

Scaillet B. and MacDonald R. A. Y. (2006) Experimental and thermodynamic constraints on the sulphur yield of peralkaline and metaluminous silicic flood eruptions. *J. Petrol.* **47**, 1413–1437.

Schmidt M. W. (2015) Melting of pelitic sediments at subarc depths: 2. Melt chemistry, viscosities and a parameterization of melt composition. *Chem. Geol.* **404**, 168–182.

Schmidt M. W. and Poli S. (1998) Experimentally based water budgets for dehydrating slabs and consequences for arc magma generation. *Earth Planet. Sci. Lett.* **163**, 361–379.

Schmidt M. W., Vielzeuf D. and Auzanneau E. (2004) Melting and dissolution of subducting crust at high pressures: the key role of white mica. *Earth Planet. Sci. Lett.* **228**, 65–84.

Shinohara H. (2013) Volatile flux from subduction zone volcanoes: Insights from a detailed evaluation of the fluxes from volcanoes in Japan. *J. Volcanol. Geoth. Res.* **268**, 46–63.

Simon A. C. and Ripley E. M. (2011) The Role of Magmatic Sulfur in the Formation of Ore Deposits. *Rev. Mineral. Geochem.* **73**, 513–578.

Singer B. S., Jicha B. R., Leeman W. P., Rogers N. W., Thirlwall M. F., Ryan J. and Nicolaysen K. E. (2007) Along-strike trace element and isotopic variation in Aleutian Island arc basalt: Subduction melts sediments and dehydrates serpentine. *J. Geophys. Res.: Solid Earth* **112**, B06206.

Skora S. and Blundy J. (2010) High-pressure Hydrous Phase Relations of Radiolarian Clay and Implications for the Involvement of Subducted Sediment in Arc Magmatism. *J. Petrol.* **51**, 2211–2243.

Smythe D. J., Wood B. J. and Kiseeva E. S. (2017) The S content of silicate melts at sulfide saturation: New experiments and a model incorporating the effects of sulfide composition. *Am. Mineral.* **102**, 795–803.

Sorbadere F., Laurenz V., Frost D. J., Wenz M., Rosenthal A., McCammon C. and Rivard C. (2018) The behaviour of ferric iron during partial melting of peridotite. *Geochim. Cosmochim. Acta* **239**, 235–254.

Spandler C., Mavrogenes J. and Hermann J. (2007) Experimental constraints on element mobility from subducted sediments using high-P synthetic fluid/melt inclusions. *Chem. Geol.* **239**, 228–249.

Spandler C., Yaxley G., Green D. H. and Rosenthal A. (2008) Phase Relations and Melting of Anhydrous K-bearing Eclogite from 1200 to 1600°C and 3 to 5 GPa. *J. Petrol.* **49**, 771–795.

Spandler C., Yaxley G., Green D. H. and Scott D. (2010) Experimental phase and melting relations of metapelite in the upper mantle: implications for the petrogenesis of intraplate magmas. *Contrib. Mineral. Petrol.* **160**, 569–589.

Syracuse E. M., van Keken P. E. and Abers G. A. (2010) The global range of subduction zone thermal models. *Phys. Earth. Planet. In.* **183**, 73–90.

Tang M., Erdman M., Eldridge G. and Lee C.-T. (2018) The redox "filter" beneath magmatic orogens and the formation of continental crust. *Sci. Adv.* **4**, eaar4444.

Tang M., Lee C.-T.-A., Chen K., Erdman M., Costin G. and Jiang H. (2019) Nb/Ta systematics in arc magma differentiation and the role of arclogites in continent formation. *Nat. Commun.* **10**, 235.

Tassara S., Reich M., Cannatelli C., Konecke B. A., Kausel D., Morata D., Barra F., Simon A. C., Fiege A., Morgado E. and Leisen M. (2020) Post-melting oxidation of highly primitive basalts from the southern Andes. *Geochim. Cosmochim. Acta* **273**, 291–312.

Thomson A. R., Walter M. J., Kohn S. C. and Brooker R. A. (2016) Slab melting as a barrier to deep carbon subduction. *Nature* **529**, 76–79.

Tollan P. and Hermann J. (2019) Arc magmas oxidized by water dissociation and hydrogen incorporation in orthopyroxene. *Nat. Geosci.* **12**, 667–671.

Tomkins A. G. and Evans K. A. (2015) Separate zones of sulfate and sulfide release from subducted mafic oceanic crust. *Earth Planet. Sci. Lett.* **428**, 73–83.

Tsuno K. and Dasgupta R. (2012) The effect of carbonates on near-solidus melting of pelite at 3GPa: Relative efficiency of H_2O and CO_2 subduction. *Earth Planet. Sci. Lett.* **319-320**, 185–196.

Vigouroux N., Wallace P. J., Williams-Jones G., Kelley K., Kent A. J. R. and Williams-Jones A. E. (2012) The sources of volatile and fluid-mobile elements in the Sunda arc: A melt inclusion study from Kawah Ijen and Tambora volcanoes, Indonesia. *Geochem. Geophys. Geosyst.* **13**, Q09015.

Wallace P. J. (2005) Volatiles in subduction zone magmas: concentrations and fluxes based on melt inclusion and volcanic gas data. *J. Volcanol. Geoth. Res.* **140**, 217–240.

Wallace P. J. and Edmonds M. (2011) The Sulfur Budget in Magmas: Evidence from Melt Inclusions, Submarine Glasses, and Volcanic Gas Emissions. *Rev. Mineral. Geochem.* **73**, 215–246.

Wang J., Xiong X., Takahashi E., Zhang L., Li L. and Liu X. (2019) Oxidation State of Arc Mantle Revealed by Partitioning of V, Sc, and Ti Between Mantle Minerals and Basaltic Melts. *J. Geophys. Res.: Solid Earth* **124**, 4617–4638.

Webster J. D. and Botcharnikov R. E. (2011) Distribution of Sulfur Between Melt and Fluid in S-O-H-C-Cl-Bearing Magmatic Systems at Shallow Crustal Pressures and Temperatures. *Rev. Mineral. Geochem.* **73**, 247–283.

Walters J. B., Cruz-Uribe A. M. and Marschall H. R. (2020) Sulfur loss from subducted altered oceanic crust and implications for mantle oxidation. *Geochem. Perspect. Lett.* **13**, 36–41.

Workman R. K. and Hart S. R. (2005) Major and trace element composition of the depleted MORB mantle (DMM). *Earth Planet. Sci. Lett.* **231**, 53–72.

Zajacz Z. and Tsay A. (2019) An accurate model to predict sulfur concentration at anhydrite saturation in silicate melts. *Geochim. Cosmochim. Acta* **261**, 288–304.

Zajacz Z., Candela P. A., Piccoli P. M. and Sanchez-Valle C. (2012) The partitioning of sulfur and chlorine between andesite melts and magmatic volatiles and the exchange coefficients of major cations. *Geochim. Cosmochim. Acta* **89**, 81–101.

Zhang H. L., Cottrell E., Solheid P. A., Kelley K. A. and Hirschmann M. M. (2018) Determination of $Fe^{3+}/\Sigma Fe$ of XANES basaltic glass standards by Mössbauer spectroscopy and its application to the oxidation state of iron in MORB. *Chem. Geol.* **479**, 166–175.

Zimmer M. M., Plank T., Hauri E. H., Yogodzinski G. M., Stelling P., Larsen J., Singer B., Jicha B., Mandeville C. and Nye C. J. (2010) The Role of Water in Generating the Calc-alkaline Trend: New Volatile Data for Aleutian Magmas and a New Tholeiitic Index. *J. Petrol.*, 2411–2444.

Associate editor: Rajdeep Dasgupta